Impact of the surface functionalization on nanodiamond biocompatibility: a comprehensive view on human blood immune cells

Laura Fusco [a, b, d, 1], Elisabetta Avitabile [c, 1], Valentina Armuzza [a], Marco Orecchioni [c], Akcan Istif [a], Davide Bedognetti [d, **], Tatiana Da Ros [a, *], Lucia Gemma Delogu [b, c, e, ***]

[a] Department of Chemical and Pharmaceutical Sciences, University of Trieste, Via L. Giorgieri 1, 34127, Trieste, Italy
[b] Fondazione Istituto di Ricerca Pediatrica Città della Speranza, Corso Stati Uniti 4, 35127, Padua, Italy
[c] Department of Chemistry and Pharmacy, University of Sassari, Via Vienna 2, 07100, Sassari, Italy
[d] Cancer Program, Sidra Medicine, Education City, Doha, Qatar
[e] Department of Biomedical Sciences, University of Padua, Via Ugo Bassi, 58/B, 35131, Padua, Italy

A B S T R A C T

Nanodiamonds (NDs) represent a class of carbon nanostructures widely investigated as promising biomedical nanotools. The possible immune system reactions indicate success or failure for any nano-system bioapplication. Moreover the assessment of the role of nanomaterial functionalization on the immune system response needs to be fully elucidated. We aimed to dissect the immunologic impact of two NDs differing for their functionalization, carboxylic acid modified NDs (NDs-COOH) and amino-functionalized NDs (NDs-NH_2), presenting a glycolic chain as spacer. We used human peripheral blood mononuclear cells (PBMCs) as model for potential biomedical scenario of NDs interaction with the human body. The ND immunologic effects were depicted toward the complex mix of PBMCs. The results showed that both functionalizations possess high hemocompatibility but NDs-COOH induced a cell viability reduction, affecting monocytes. The ND impact was depicted through immune activation markers, immune-response gene expression and cytokine secretion analysis. Immune markers confirmed the impact on monocytes, more evident for NDs-COOH. Both NDs affected the immune response, however NDs-COOH showed more prominent responses, evoking pronounced regulation of immune-modulatory transcripts. The cytokine analysis confirmed gene expression data for proinflammatory cytokines related to the innate response.

Our findings reveal that NDs decoration with an amino-terminating chain enhances their immunologic compatibility.

1. Introduction

In the era of nanotechnology, nanomedicine represents the field devoted to the biomedical applications of engineered materials [1–4]. Among them, carbon-based materials (CBMs), such as graphene, carbon nanotubes (CNTs) and nanodiamonds (NDs), have been extensively explored as promising therapeutic and diagnostic nanotools. However, their potential use in medicine remains still limited due to the controversial debate on their biocompatibility and safety. Moreover, the biological effects appear to be strongly related to the different type of CBMs and to their functionalities and physical parameters [5,6].

NDs are a class of CBMs consisting of nano-sized tetrahedral networks, which have shown a superior biocompatibility when compared to other members of the nanocarbon family [7–10]. NDs have attracted the interest of the scientific community thanks to their outstanding optical characteristics, magnetic properties [11–13] extreme hardness [14], and capability of bio-

* Corresponding author.
** Corresponding author.
*** Corresponding author. Institute of Pediatric Research, Foundation City of Hope, Corso Stati Uniti 4, 35127, Padua, Italy.
E-mail addresses: dbedognetti@sidra.org (D. Bedognetti), daros@units.it (T. Da Ros), luciagemma.delogu@unipd.it, ldelogu@uniss.it (L.G. Delogu).
[1] These authors contributed equally to the present work.

functionalization [15,16]. All these unique characteristics make them suitable candidates for biomedical applications [17]. Among these, several are in the context of cancer, from colon cancer [18], pancreatic cancer [19], glioblastoma [20] to breast cancer [21] as well as in bioimaging [22], tissue engineering [23], and drug delivery [24–26], and they are proposed also as key components for cosmetics and sunscreen formulations [16].

However, a critical step for safe applications of nanomaterials as medical and personal care tools is represented by the assessment of their impact on the immune system. Indeed, the immune system governs every aspect of our health, and represents the body defense barrier from noxious agents. This is of great importance, especially considering that some of the most effective NDs biomedical applications, such as controllable drug delivery and tracing, assume their intravenous injection. Studies aimed at exploring the effect of NDs on immune cells are limited [27–29]. Some of them reported the absence of immune responses induced by NDs *in vitro* on primary human macrophages and *in vivo* after injection in blood in mice suggesting their suitability as anti-inflammatory drug delivery platforms directly targeting macrophages through phagocytosis [27–29]. On the other hand, some findings showed their impact on the immunologic activation using mouse leukaemic monocyte macrophage cell line (Raw264.7 cells) [30]. This discrepancy is due in part to the specific physicochemical proprieties of the different types of NDs tested. In fact differences in morphology, dimensions, and defects due to the growth process [31] can have a key role on the biological impacts. Among the most conventional methods used for NDs manufacturing, detonation represents a suitable technique for industrial scale production. Compared to other protocols to prepare NDs, such as the high temperature/high pressure (HTHP) method, detonation leads to smaller dimension (around 5 nm) and less lattice fluorescent defects to the resulting diamond particles, named as detonation-produced nanodiamonds (DNDs).

To enhance their fluorescence or other proprieties, DNDs are often modified with organic molecules [32–35]. The surface of pristine NDs usually presents functional moieties, such as hydroxyl, carboxyl and ketone groups [36–38]. The large number of oxygen-containing functions allows the customized design of NDs, making their surface tailorable for specific decorations to modify or expand their properties according to the biomedical application requirements. In particular, the amino-functionalization enhances dispersion and interfacial interactions of CBMs and we have previously shown that the amino-functionalization of other CBMs, such as graphene and CNTs, has a significant impact on the downstream effect on immune cells, at the same time enhancing their immune compatibility [39,40].

Here, we aimed to understand how these nanomaterials can modulate the immune response depending on their different surface modifications with amino-functional groups, a leading bridge for the development of future biomedical perspectives. To explore this complex aspect, we report a comprehensive analysis on a wide variety of primary human immune cell interactions with two ND derivatives differing for their functionalization, NDs-COOH, presenting on the surface carboxylic groups, and NDs-NH_2, where the carboxylic groups have been used to attach amine-terminating oxyethylene chains. Human erythrocytes (red blood cells, RBCs) and the pool of human peripheral blood mononuclear cells (PBMCs) from healthy donors were used as they represent a more close-to-human *in vivo* condition as compared to cell lines or animal models. To have a comprehensive view on the adaptive and innate response, the assays were carried out on four different PBMC subpopulations by gating them via specific antibodies able to recognize and differentiate the major immune subpopulations: T cells, B cells, natural killer (NK) cells, and monocytes. After evaluating the hemocompatibility of NDs and their impact on immune cell late apoptosis and necrosis, their ability to be internalized into the immune cells, as well as their effect on cell activation, genomic impact and cytokine release, was determined following cell exposure to NDs.

We demonstrated that the effects of NDs on the immune system strongly depend upon their surface chemistry. In particular, our results suggest that functionalization with amino-terminating chains has a key role in enhancing the NDs immune compatibility, therefore representing a key strategy for their clinical translational applications.

2. Experimental section

2.1. Synthesis of NDs derivatives

Pristine NDs (Nanodiamond powder, > 98% purity, cubic phase, 4–5 nm primary particle size, Adamas Nanotechnologies, 200 mg) were dispersed in 200 mL of sulfonitric mixed acid. After a short sonication using a Branson 2510 water bath sonicator, the reaction mixture was stirred at 80 °C for 12 h. Subsequently, NDs were filtrated using an Omnipore membrane (JVWP, 0.1 μm) and washed with water until neutral pH was obtained. Then, the solid was washed with DMF, MeOH, AcOEt, and Et_2O and dried under vacuum, resulting in 200 mg of NDs-COOH. The sample was then characterized by transmission electron microscopy (TEM), thermogravimetric analysis (TGA), Fourier transform infrared spectroscopy (FT-IR), atomic force microscope (AFM) and Raman spectroscopy. Assuming that the weight loss at 500 °C is only attributable to the carboxylic acid decomposition, from TGA analysis the degree of functionalization results 405 μmol g^{-1}. 40 mg of NDs-COOH were dispersed in 20 mL of dichloromethane, and the suspension was cooled at 0 °C and purged with nitrogen for few minutes. Later on, a solution of 2-(1H-benzotriazole-1-yl)-1,1,3,3-tetramethylaminium tetrafluoroborate (TBTU; 103 mg, 0.32 mmol) and N,N-diisopropylethylamine (DIPEA, 411 μL, 2.36 mmol) in dichloromethane (20 mL) was added and the mixture was stirred 1 h at 0 °C. N-Boc-amino-diethoxy-ethylamine (80 mg, 0.32 mmol) was added into the suspension of NDs and the reaction mixture was stirred at r.t. overnight. Then the NDs were filtrated using an Omnipore membrane (JVWP, 0.1 μm) and washed with DMF, water and re-dispersed in 37 mL of HCl (4 M) in dioxane to deprotect the Boc-group. The mixture was stirred overnight at r.t. and then the NDs were filtrated and washed with H_2O, DMF, MeOH, AcOEt and Et_2O and dried under vacuum, resulting in 37 mg of NDs-NH_2, with a calculated degree of functionalization of 540 μmol g^{-1} (from TGA at 500 °C). A deoxygenated suspension of NDs-NH_2 (15 mg), fluorescein isothiocyanate (FITC, 32 mg) and DIPEA (0.03 mL) in DMF (4.1 mL) was stirred at r.t. for 16 h and then the reaction mixture was filtrated and NDs were washed with DMF, water, MeOH, AcOEt and Et_2O and dried under vacuum, recovering 10 mg of NDs-FITC with a calculated degree of functionalization of 133 μmol g^{-1} (from TGA at 500 °C).

2.2. Chemical characterization

2.2.1. Raman

Raman spectra were recorded using an inVia Renishaw spectrometer equipped with a 532 nm laser. For the analysis about 0.5 mg of each sample were dispersed in 1 mL of DMF and 3 drops of the suspension were deposited on a silicon wafer and let them dry.

2.2.2. TGA

TGA was recorded using a Q500 (TA Instruments), in inert atmosphere (N_2). The equilibration at 100 °C for 20 min was followed by a ramp of 10 °C/min up to 800 °C. About 1 mg of compound was used for each analysis. The degree of functionalization, expressed in μmol/g, is calculated as following:

$$\frac{\mu mol}{g} = \frac{\text{weight loss } (\%) \cdot 10000}{\text{Molecular weight of functional group}}$$

where the weight loss (%) is given from the difference between the weight loss of the compound and the weight loss of the precursor nanomaterial. The used values correspond to the weight loss that took place at 500 °C, as arbitrary temperature.

2.2.3. IR spectra

IR spectra were recorded on a PerkinElmer spectrum RX I FT-IR System, pellets were prepared mixing about 1 mg of the sample with the KBr, previously dried.

2.2.4. TEM

TEM analyses were performed using a TEM Philips EM208 with an accelerating voltage of 100 kV. For the analysis 0.1 mg of each sample were dispersed in 1 mL of water and one drop of the suspension was deposited on a TEM grid (200 mesh, Nichel) and dried under vacuum.

2.2.5. Fluorescence spectra

Fluorescence spectra were recorded on a Cary Eclipse Fluorescence Spectrophotometer (Agilent Technologies), using quartz cuvettes (path length = 1 cm).

2.2.6. AFM

AFM images were recorded on an Agilent Technologies 5500 scanning probe microscope, operating in acoustic AC AFM mode and WSxM R5 software was used to process the images. The samples concentration was 0.2 mg mL^{-1} in water and the same suspension volume was deposed on silicon wafer and dried in air.

2.3. Biological experiments

2.3.1. PBMC isolation and immune cell subpopulation gating

Human PBMCs were isolated from heparin anti-coagulated venous blood from healthy consenting adults using a standard buffy coat protocol. PBMCs were isolated from participants who had given informed consent for the use of the "Centro Trasfusionale, Sassari, Sardinia, Italy" and research activities within the University of Sassari. The Nanobiotechnology lab of the University of Sassari obtained the approval from the "Centro Trasfusionale, Sassari, Sardinia, Italy" to handle the discarded products of buffy coat collection. The donors were not needed to complete the specific informed consent related to this study because all cells used here were obtained from normally discarded products, the donors had approved for the use of their cells in research projects and the donors were completely de-identified, so these studies were exempt from further approval. The recruited healthy donors were generally ranged in age from 25 to 50 years old. Human PBMCs were isolated from whole blood samples using Ficoll-Plaque™ PLUS (GE Healthcare) high-density gradient centrifugation at 1:1 ratio. PBMCs were cultured in RPMI 1640 medium completed with 10% of inactivated fetal bovine serum (Invitrogen) and 1% of pen/strep mixture (Invitrogen). The homogenous solution with NDs and sterile ultrapure water was prepared (1 μg mL^{-1}). NDs were sonicated for 40 min with a Branson 3200 water bath sonicator before PBMC incubation. After NDs treatment and PBS washing, major immune cell populations were identified by flow cytometry according to the expression of specific cell surface markers (clusters of differentiation [CD]) that were detected with fluorescently labeled monoclonal antibodies. Fluorescein isothiocyanate (FITC)-, phycoerythrin-, peridinin chlorophyll protein-, or allophycocyanin-conjugated anti-CD3 (SK7 clone), anti-CD4 (SK3 clone), anti-CD8 (SK1 clone), anti-CD14 (Mf9 clone), anti-CD16 (3G8 clone), anti-CD20 (L27 clone), anti-CD69 (L78 clone), anti-CD25 (2A3 clone), anti-HLA DR (L243 clone), anti-CD161 (DX12 clone) were purchased from BD Biosciences (Mountain View). Cell gating was performed using the above mentioned antibodies to recognize the major population of PBMCs: CD3+/CD4+ and CD3+/CD8+ for T cells, CD20+ for B cells, CD14+ for monocytes and CD16+/CD3- for NK cells. To assess the expression of cell surface markers, cells were washed twice with 0.5% bovine serum albumin in PBS pH 7.2 and were incubated for 20 min in dark conditions with fluorochrome-conjugated monoclonal antibodies. Experiments were performed in triplicates using at least three different healthy donors' blood samples.

2.3.2. Hemocompatibility assays

Fresh human heparinized whole blood was obtained from healthy volunteer donors. RBCs were purified from blood by centrifugation at 200×*g* for 5 min to remove serum. RBCs were then washed in sterile isotonic PBS 1X five times and diluted 10X with the same solution. To determine the hemolytic activity of NDs, nanoparticles suspensions (1 mg mL^{-1}) were prepared with deionized water (DDW) and added to diluted RBC suspension (0.1 mL, ~2 × 10^8 cells mL^{-1}) at different concentrations (5, 25, 50, and 100 μg mL^{-1}) and for different times of exposure (6, 12, and 24 h) at r.t. Then the preparation was subjected to vortex. A microplate reader (Thermo Scientific) was used to measure the absorbance of hemoglobin release in the supernatant at 570–690 nm.

Biocompatibility test was provided on human PBMCs incubated in a 24-well plate (25 × 10^4 cells/well) with 50 μg mL^{-1} for 6 and 24 h. Cells were then collected and cell pellets were suspended in a sterile isotonic PBS 1X for sufficient conductivity during Scepter cell counting. Each sample was incubated for 1 min with EtOH 70% (v/v) as a positive control and then suspended as previously described. Data were analyzed by Scepter 2.0 software to determine the concentrations and relative cell frequencies for lymphocyte and monocyte fractions.

2.3.3. Viability assay

Cell viability was evaluated by flow cytometry (FACS Canto II, BD Biosciences, Mountain View, CA, USA) using 7-amino-actinomycin D (7-AAD, BD Bioscience, San Josè, CA, USA). Briefly, PBMCs (25 × 10^4 cells/well) were exposed to increasing concentrations of NDs (5, 25, 50, and 100 μg mL^{-1}) for 6, 12, and 24 h. EtOH (70% v/v) was used as positive controls. Cells were stained with fluorescent antibodies for 20 min in the dark at r.t. and then analyzed by flow cytometry.

2.3.4. Uptake of NDs

To analyze NDs uptake, PBMCs (25 × 10^4 cells/well) were seeded in 24-well plates and exposed to increasing concentration of NDs-FITC (5, 25, 50, and 100 μg mL^{-1}) for 24 h. After the staining with cell subset-specific antibodies for 20 min in the dark, cells were washed with PBS 1X solution and flow cytometry measurements were performed using a FACS Canto II cytometer (BD Biosciences, Mountain View, CA, USA). The incubation experiment was repeated exposing cells to 50 μg mL^{-1} of NDs-FITC for 24 h and, in this case, cells were washed twice with PBS 1X, fixed with 1 mL of 4% paraformaldehyde/PBS 1X fixation buffer and incubated with

propidium iodide (PI) solution. After 15 min, cells were washed and suspended in PBS 1X solution. A microscope glass-slide with treated PBMCs was prepared using Mowiol 4–88 (Sigma-Aldrich). Finally, the samples were imaged by confocal microscopy (Leica TCS SP5 confocal microscope). Fluorescein signal was acquired using the 488 Argon blue laser line and then analyzed with LAS lite 170 image software.

2.3.5. Activation marker assay

PBMCs differentiation was evaluated by the expression of specific differentiation markers (CD25, CD80, and CD86). Subsequently, PBMCs were stained with specific fluorescent monoclonal antibodies (Abs) as immune cell population and cell differentiation markers: 2A3 clone, specific for CD25; 1610-A1 clone, specific for CD80; and with 2331 clone, specific for CD86, according to manufacturer's instructions (BD-Bioscience Mountain View, CA, USA). PBMCs (5×10^5 cells) were seeded in 96-well plates and exposed to NDs-COOH or NDs-NH_2 (50 μg mL^{-1}) for 24 h. Subsequently, cells were collected and stained with fluorochrome-conjugated monoclonal antibodies as previously described. Monocytes subpopulation was selected by gating $CD14^+$ cells. Concanavalin A (ConA; 10 μg mL^{-1}) or lipopolysaccharide (LPS, 2 μg mL^{-1}) were used as positive control (Sigma-Aldrich, St. Louis, Missouri, USA).

2.3.6. Immune gene array

PBMCs (5×10^5 cells) were seeded in 96-well plates and exposed to NDs-COOH or NDs-NH_2 (50 μg mL^{-1}) for 24 h. Subsequently, cells were collected and washed with ice-cold PBS. Total RNA was extracted by TriZol Reagent (TriZol, Invitrogen; Carlsbad, CA, USA), following manufacturer's instructions. After measuring purity and concentration using a Nanodrop Spectrometer (Nanodrop® ND1000), RNA was retrotrascripted by Polymerase Chain Reaction (PCR) using Superscript IV Reverse Transcriptase kit (Life Technologies; Milan, Italy) according to manufacturer's protocol. To quantify the expression of 84 specific immune genes, RT2 Profiler PCR Array (PAHS-052ZD, Superarray Bioscience Corporation, Frederick, MD) was applied. Amplifications on plates were set using a Real-Time instrument (CFX96 Bio-Rad).

2.3.7. Cytokine secretion assay

PBMCs (5×10^5 cells) were seeded in 96-well plates and exposed to NDs-COOH or NDs-NH_2 (50 μg mL^{-1}) for 24 h. Subsequently, cell culture supernatants from PBMCs were collected to quantify secretion of interleukin (IL)-1β, IL-2, IL-6, IL-4, IL-10, tumor necrosis factor (TNF)-α, interferon (IFN)-γ, by a MILLIPLEX MAP 7-plex Cytokine Kit (HCYTOMAG-60K-07, Millipore, Billerica, MA) following manufacturer's instructions.

2.3.8. Statistical analysis

Data analyses were performed using Student's t-test (* indicates $p < 0.05$ and ** indicates $p < 0.01$). Flow cytometry data were analyzed using FACS Diva software (BD-Bioscience Mountain View, CA, USA). All experiments were performed at least in triplicate. Immune gene array data were calculated by the comparative threshold cycle method. Data were analyzed with RT2 profiler PCR array data analysis software (http://pcrdataanalysis.sabiosciences.com/pcr/arrayanalysis.php). Fold change ($2^{-\Delta\Delta Ct}$) is the normalized gene expression ($2^{-\Delta Ct}$) in the test sample divided by the normalized gene expression ($2^{-\Delta Ct}$) in the control sample. Fold changes are transformed in fold regulations to allow matrix symmetry and facilitate data interpretation. For fold change >/ = 1, fold regulation corresponds to fold change. For fold change <1, fold regulation is calculated as - 1/fold change. Multiplex ELISA assay on human PBMCs were performed in samples from at least two different healthy donors.

3. Results and discussion

3.1. Synthesis and characterization of functionalized NDs: NDs-COOH and NDs-NH_2

Commercial pristine DNDs, characterized by spherical shape and small and homogeneous dimensions (primary particle size of 4–5 nm), were selected as reference for this study, varying their surface by means of chemical treatment, with the introduction of carboxylic groups (NDs-COOH), followed by the appendage of hydrophilic chains terminating with a primary amine.

To obtain NDs-COOH, the commercial DNDs were oxidized by means of the sulfonitric mixture to increase the presence of carboxylic acid functions on their surface and to render the material more dispersible in polar solvents (Fig. 1). The resulting NDs-COOH were allowed to react with TBTU to activate the carboxylic groups and then were treated with N-Boc-amino-diethoxyethylamine, to give the corresponding amide, which was directly deprotected by acidic treatment. Part of the obtained NDs-NH_2 was labeled with FITC, to prepare the fluorescein-conjugated NDs (NDs-FITC).

NDs-COOH, NDs-NH_2, and NDs-FITC were thoroughly characterized using different techniques as TGA, FT-IR spectroscopy, TEM, and AFM before to determine the influence of their surface chemical composition on their biocompatibility.

Initially, to ensure that the acidic treatment performed with the sulfonitric mixture did not alter the NDs internal structure, the Raman spectra of pristine materials and NDs-COOH were compared (Fig. S1A). Their profiles resulted almost superimposable, with the presence of strong bands at around 1326 cm^{-1}, corresponding to the diamond peak, and 1620 cm^{-1}. At about 1740 cm^{-1} NDs-COOH spectrum showed a shoulder, attributable to the C═O of the surface functional groups.

NDs functionalization was then investigated by TGA under non-oxidizing condition (nitrogen atmosphere) and in a temperature range from 100 to 800 °C. As appreciable from Fig. 2A (and Fig. S1B), the obtained results revealed an increase in thermolabile functions for NDs-COOH compared to pristine materials, confirming the oxidation. The subsequent introduction of the hydrophilic chains was confirmed by a weight loss of about 9% at 500 °C, corresponding to a degree of functionalization of 540 μmol g^{-1}. The discrepancy of this value with respect to the content of carboxylic residue is attributable to the fact that a small percentage of epoxides can be still present on the ND surface and the amines react with them and the degree of functionalization results to be higher than the carboxylic functionalization. The introduction of the fluorescein in derivative NDs-FITC was also confirmed by TGA, with an increase of weight loss corresponding to a degree of functionalization of 133 μmol g^{-1}, as well as by fluorescence spectroscopy (Fig. S1C). From the FT-IR spectra (Fig. S1D) it is possible to appreciate the presence of the C–O–H in plane bending at 1430 cm^{-1} in pristine NDs and NDs-COOH, while for NDs-NH_2 and NDs-FITC the presence of ethers is confirmed by the detection of two strong signals at 1170 cm^{-1}, attributable to the C–O–C stretching.

TEM images (Fig. 2B) were acquired for NDs-COOH and NDs-NH_2. For each material, a suspension in water (100 μg mL^{-1}) was prepared and deposited on the TEM grids. The images herein reported revealed the presence of aggregates for both materials, however, the aggregation resulted much more pronounced for NDs-COOH, compared to NDs-NH_2. In the latter the sample results more homogeneously dispersed as appreciable from Fig. 2B. To deeper characterize the observed clusters, AFM analysis was performed on NDs-COOH and NDs-NH_2 (Fig. 2C). For each material, a drop casting preparation in water (200 μg mL^{-1}) was obtained and deposed on silicon wafer substrates. The recorded topographic

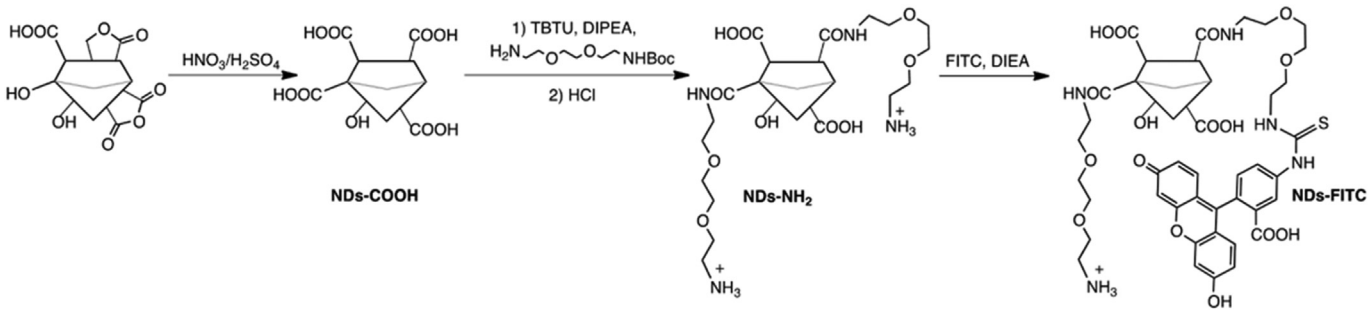

Fig. 1. Functionalization of NDs. Schematic representation of ND functionalization. The number of functional groups on the NDs is arbitrary and the real proportion of the drawn structures is not taken into account.

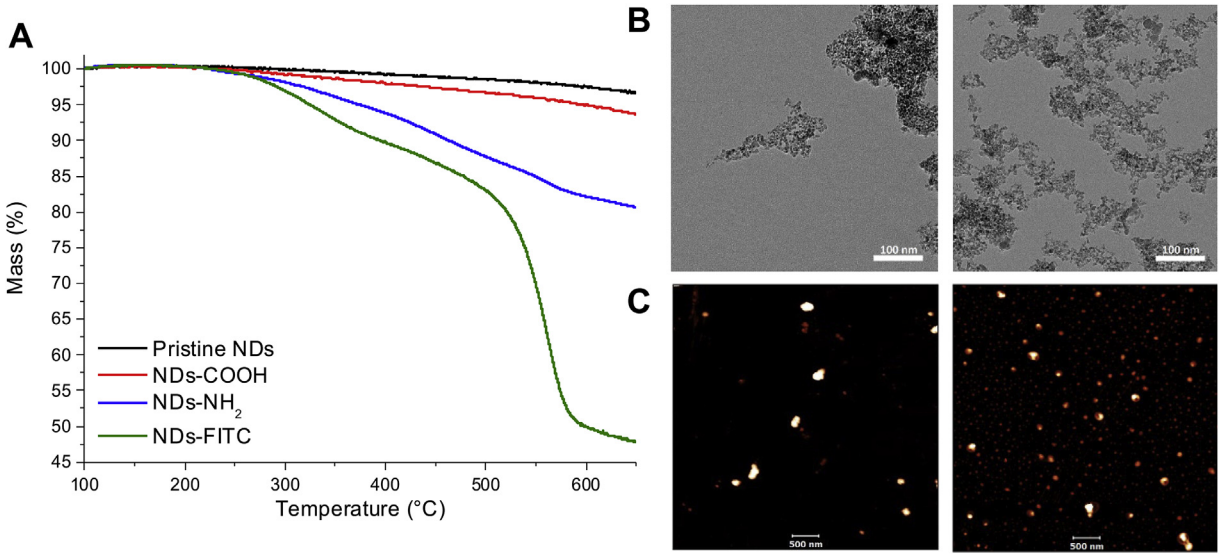

Fig. 2. Characterization of NDs. (A) TGA profile of pristine NDs (black line), NDs-COOH (red line), NDs-NH_2 (blue line), and NDs-FITC (green line), obtained by TGA analyses performed in inert atmosphere (nitrogen); **(B)** Bright-field TEM images of NDs-COOH (left side) and NDs-NH_2 (right side), dispersed in water (100 μg mL^{-1}); **(C)** AFM topographic images of NDs-COOH (left side) and NDs-NH_2 (right side) dispersed in water (200 μg mL^{-1}) on silicon wafer. (A colour version of this figure can be viewed online.)

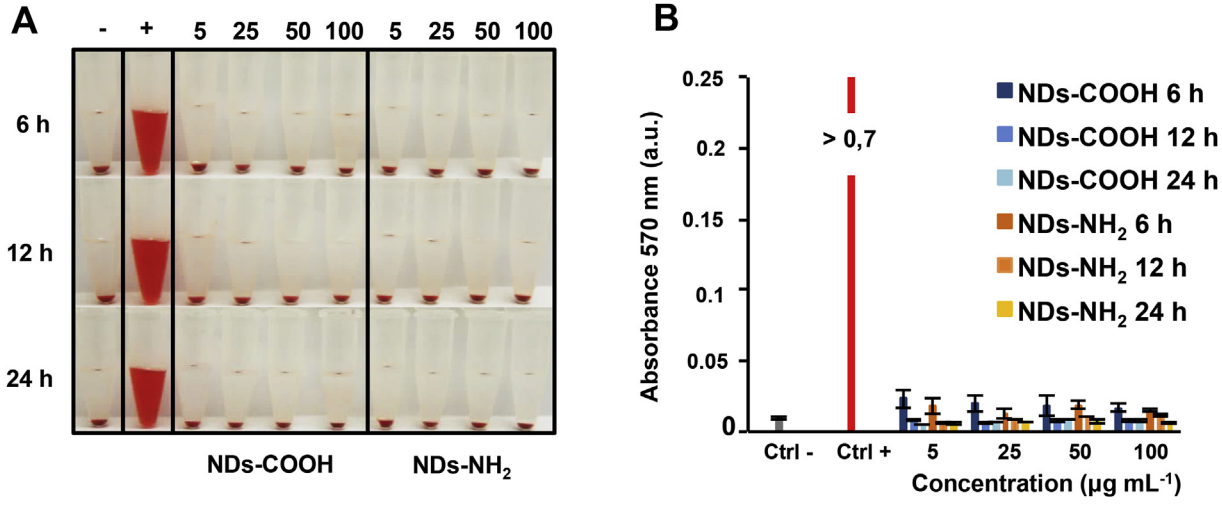

Fig. 3. Hemocompatibility. Hemolysis test on human RBCs after exposure to increasing concentrations (5, 25, 50, and 100 μg mL^{-1}) of NDs-COOH or NDs-NH_2 for 6, 12, and 24 h. **(A)** Pictures of human RBCs treated with NDs-COOH or NDs-NH_2 at the different doses and time points. PBS and DDW were used as negative (−) and positive (+) control, respectively; **(B)** Hemolysis was evaluated based on absorbance at 570 nm by spectrophotometer. (A colour version of this figure can be viewed online.)

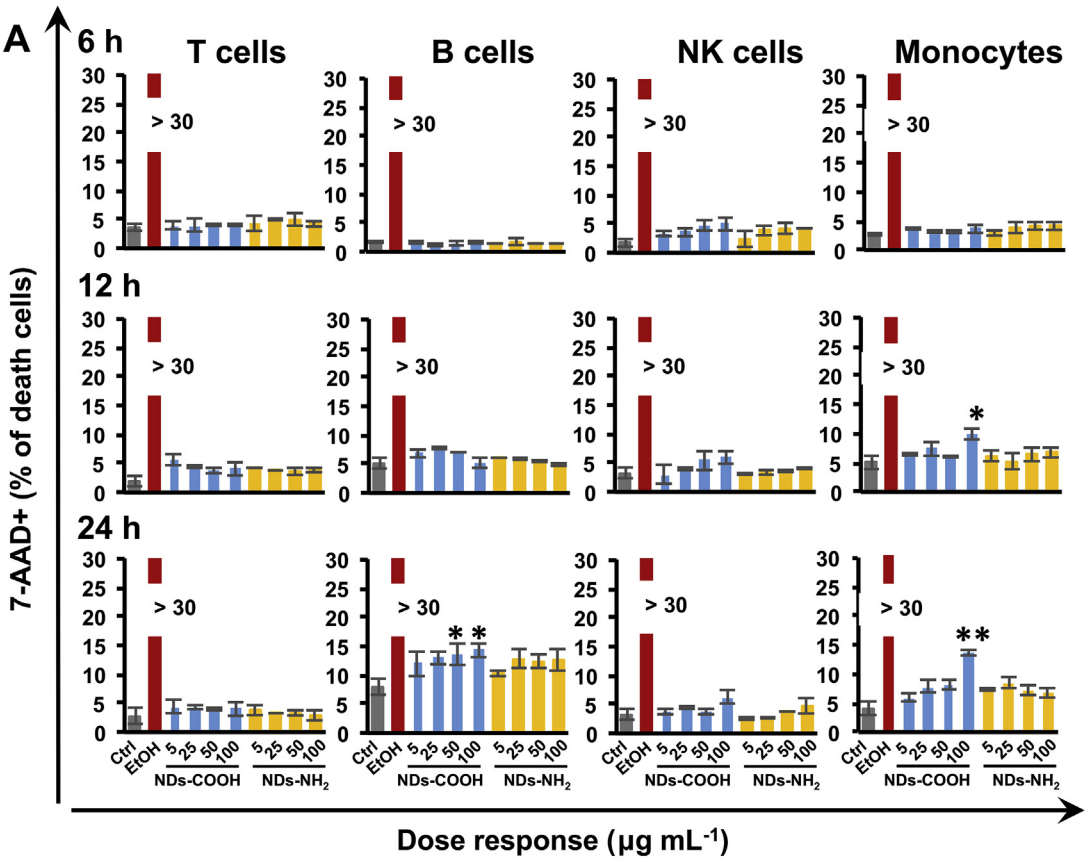
A
6 h
12 h
24 h
T cells
B cells
NK cells
Monocytes
> 30
*
**
7-AAD+ (% of death cells)
Ctrl
EtOH
5
25
50
100
NDs-COOH
NDs-NH2
Dose response (µg mL-1)

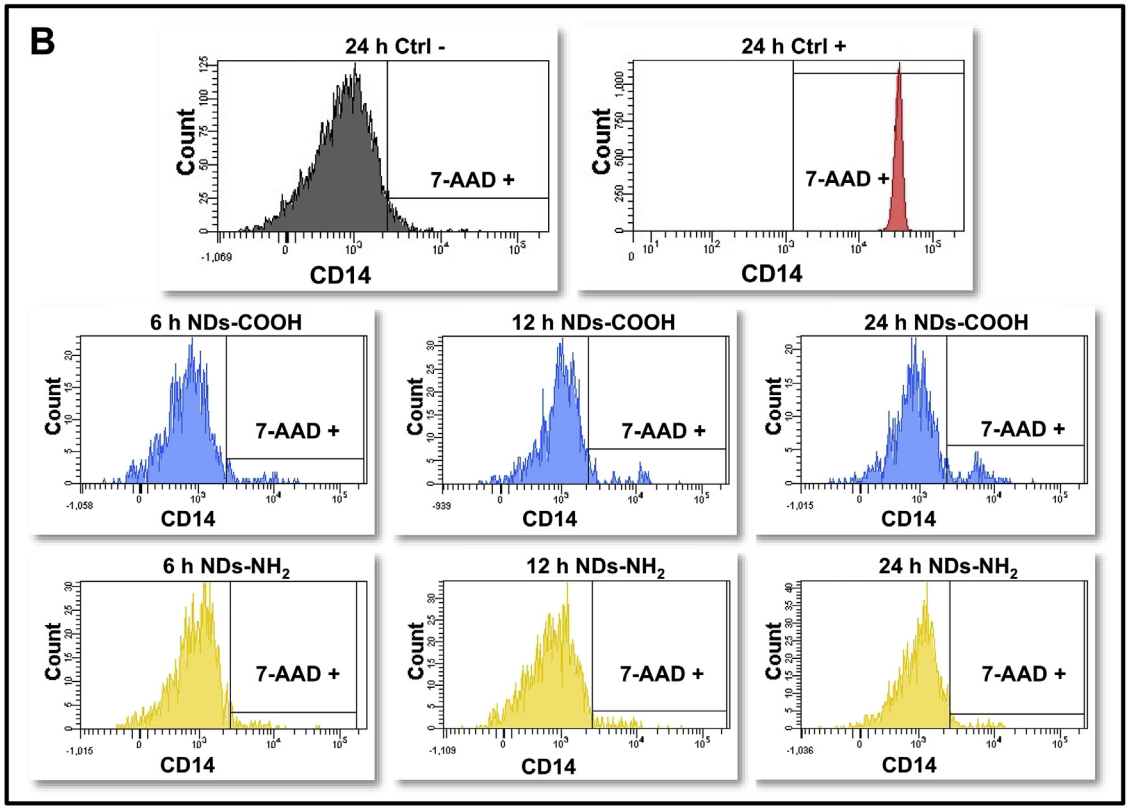
B
24 h Ctrl -
24 h Ctrl +
6 h NDs-COOH
12 h NDs-COOH
24 h NDs-COOH
6 h NDs-NH2
12 h NDs-NH2
24 h NDs-NH2
Count
7-AAD +
CD14

images showed that the aggregates formed by NDs-NH_2 were significantly more frequent and smaller, compared to NDs-COOH clusters (See Fig. S1E). In fact in the latter case only few small structures were found and the main population consisted in big aggregates, with mean dimension of more than 30 nm for more then the 60% of the measured aggregates, as appreciable from Fig. 2C, left panel. These findings are in line with qualitative experiments on the stability of suspension prepared with 1 mg of NDs in 1 mL of water, demonstrating that the NDs-NH_2 were less prone to precipitate, staying in suspension more the 48 h (data not shown).

3.2. Hemolytic activity toward human RBCs

Initially, to evaluate the blood compatibility of NDs, their hemolytic activity was investigated by means of hemoglobin release after exposure of human RBCs to increasing NDs-COOH or NDs-NH_2 concentrations (5, 25, 50, and 100 μg mL^{-1}) for 6, 12, and 24 h. Untreated cells and treatment with distilled deionized water (DDW) were used as negative and positive control, respectively. Fig. 3A shows human RBCs treated with NDs-COOH or NDs-NH_2. The pellet at the bottom of the tubes corresponds to intact RBCs precipitated after centrifugation, while the supernatant color indicates the release of hemoglobin from RBCs: the darker is the color, the greater is the amount of released hemoglobin. The hemolysis was then evaluated spectrophotometrically at the fixed absorbance wavelength of 570 nm. NDs-COOH and NDs-NH_2 did not induce any significant hemolytic activity towards RBCs at any concentration and exposure time tested (Fig. 3B) compared to the positive control DDW.

The obtained results are line with previous studies demonstrating the long-term stability and biocompatibility of NDs in rats and human RBCs for their possible applications as contrast agents in cancer therapy, mapping sentinel lymph nodes *in vivo* [27,41]. On the contrary, in contrast with our observation, Mitura *et al.* reported the hemolytic activity of commercial DNDs (inducing hemolysis at 40 μg mL^{-1}) after 10 min incubation, by the observation of spherical shape erythrocytes (spherocytes) [42]. This different behavior could be due to the absence of further functionalization and the higher agglomerate size in aqueous solutions of the DNDs used in the study (200 nm).

On the whole, our results suggest a high hemocompatibility of NDs, yielded by both ND surface modifications, highlighting their safety for RBCs compared to other CBMs, such as graphene oxide, able to induce hemolysis already at a concentration of 25 μg mL^{-1} [43].

3.3. Viability on immune cell subpopulations

The effects of NDs-COOH and NDs-NH_2 were evaluated on PBMC viability, using the 7-amino-actinomycin D (7-AAD) staining, a chemical compound with strong affinity for DNA, able to penetrate through the compromised membranes of late apoptotic and necrotic cells which allow the passage of the dye into the nucleus [44] (Fig. 4). PBMCs were exposed to increasing concentrations of NDs-COOH or NDs-NH_2 (5, 25, 50, and 100 μg mL^{-1}) for 6, 12, and 24 h and T, B NK cells and monocytes were analyzed by flow cytometry. Untreated cells and ethanol (EtOH) 70% (v/v) were used as negative and positive control, respectively. Fig. 4A shows the effects on viability of NDs-COOH and NDs-NH_2 on the different cell subpopulations, compared to the negative control. After 6 h exposure, NDs-COOH and NDs-NH_2 did not induce any significant effect on cell population viability. Starting from 12 h exposure, a reduction of monocytes viability was observed only at the highest concentration (100 μg mL^{-1}) of NDs-COOH (10% of mortality) ($p < 0.05$), which became more evident ($p < 0.01$) increasing the exposure time up to 24 h (12% of mortality). Moreover, 24 h exposure to 50 and 100 μg mL^{-1} of NDs-COOH was able to significantly ($p < 0.05$) affect also B cells viability (13 and 14% of mortality, respectively). On the contrary, NDs-NH_2 did not exert any significant effect on immune cell subpopulations viability at any dose and time of exposure applied in this study, demonstrating the role of NDs amino functionalization on their immune biocompatibility.

Considering that monocytes showed to be the most affected immune cell subpopulation, the specific impact of NDs-COOH and NDs-NH_2 highest concentration (100 μg mL^{-1}) was further analyzed on this cell subset after 6, 12 and 24 h exposure, using a time response flow cytometry assay by a CD14+ gating (Fig. 4B). Untreated PBMCs and EtOH 70% (v/v) were used as negative and positive control, respectively. Notably, compared to negative control, flow cytometry plot of CD14+ monocytes confirmed the higher impact of NDs-COOH compared to NDs-NH_2 after 12 ($p < 0.05$) and 24 h ($p < 0.01$) exposure (Fig. 4B). These observations suggest a role for the NDs decoration on their immune compatibility. Indeed, the functionalization is likely able to modulate the material aggregation state, which can be a consequent player for the immune compatibility. In fact, it has been reported that several parameters can influence the toxicity of materials, including chemical composition, surface charge, shape, solubility, and the material aggregation state [6,45,46]. In particular, it has been demonstrated that the larger aggregates of nanomaterials can be more cytotoxic than the smaller ones [47]. In agreement with this data, as shown by the TEM and AFM images, the presence of aggregates resulted much more pronounced for NDs-COOH, compared to NDs-NH_2. Therefore, this finding could explain the higher impact observed for NDs-COOH on immune cells. Moreover, it is likely possible that the different functionalization may influence the formation of the so-called bio-corona, consisting in the coating of nanomaterials with biomolecules in biological environment (e.g., albumin, the major FBS component), which plays a critical role in the subsequent toxicological impact [45]. Indeed, the surface properties can have a key role in determining the bio-corona formation [48]. However, despite it has been reported that positively and negatively charged NDs can display different electrostatic interactions modulating the protein adsorption conformation of small proteins (lysozyme), only minor conformational changes have been observed for albumin monolayer on the surface of NDs [49]. Overall, these results are in line with our previous observation on the immune impact of differently functionalized CNTs and graphene oxide [50–52]. Moreover, similar to our data, a very recent study exploring the impact of amino- and carboxylic acid-decorated NDs on a human macrophage cell line (i.e., PLB-985 cells) highlighted the different effects exerted by the two materials, revealing the higher reduction of cell viability induced by carboxylated NDs compared to amino-functionalized, starting from 50 μg mL^{-1} [19].

Fig. 4. Viability assay on human *ex vivo* immune cells. PBMCs were exposed to increasing concentrations (5, 25, 50, and 100 μg mL^{-1}) of NDs-COOH or NDs-NH_2 for 6, 12 and 24 h or left untreated; EtOH (70% v/v) was used as positive control. Cells were stained with 7-AAD and cluster of differentiation markers (CD) specific for four immune populations and then analyzed by flow cytometry. **(A)** Percentage of death cells (7-AAD positive cells, 7-AAD+) of T cells, B cells, NK cells and monocytes treated in dose response with NDs. Statistical significance is indicated by (*, $p < 0.05$), (**, $p < 0.01$); **(B)** Percentage of total monocytes (left side) and 7AAD + positive (right side) after 6, 12 and 24 h exposure to 50 μg mL^{-1} of NDs-COOH or NDs-NH_2. Untreated PBMCs and EtOH (70% v/v) were used as negative (grey) and positive control (red), respectively. The analyses were performed at least in triplicate. (A colour version of this figure can be viewed online.)

The obtained findings, showing no toxicity of amino functionalized NDs even at high concentrations, suggest the suitability of this functionalization to improve their immune-biocompatibility. Moreover, the differential aggregation state may explain also the higher impact on monocytes. Indeed, due to their phagocytic activity, monocytes are the blood cell population type more prone to internalize the NDs. As for any other nanoparticle and foreign molecule, the uptake can consequently affect the cells, and monocytes in particular, in terms of cell viability. Our hypothesis is that the impact of NDs on monocytes can be related to the specific uptake of NDs by these cells. To test our hypothesis, as next step, we tested the NDs uptake on PBMCs and their cell subpopulations.

3.4. Uptake by human peripheral blood mononuclear cells and the immune subpopulations

The biocompatibility and the high uptake rate of fluorescent NDs have been reported using cell lines and animal models [53,54]. Suarez-Kelly *et al.* revealed the immune cell internalization of NDs *in vitro* using macrophages and natural killer cell lines [55]. A complete study including all the main immune cell subpopulations and using primary human immune cells is still lacking. Therefore, we evaluated NDs internalization into four immune cell types from human peripheral blood.

To this end, PBMCs were exposed to increasing concentrations of NDs-FITC (5, 25, 50, and 100 μg mL^{-1}) for 24 h. Immune cells were stained using different specific fluorescent monoclonal antibodies to detect the four major PBMC cell subpopulations: T cells, B cells, natural killer (NK) cells and monocytes. Flow cytometry analyses indicated a different ability of immune cell populations to internalize fluorescent NDs in a dose-dependent manner (Fig. 5A). The fluorescence signal of NDs-FITC was significantly higher in monocytes compared to T cells, B cells, and NK cells, already starting from 5 μg mL^{-1}. At the highest tested concentration (100 μg mL^{-1}), the fluorescence signal rate of NDs internalized into monocytes was equal to 28%, compared to the untreated control. Among lymphocytes, B-cells showed the highest uptake rate of NDs (5% after exposure to 100 μg mL^{-1}), representing the second most efficient cell subpopulation in terms of cell internalization among the immune cells analyzed. Intriguingly, the uptake ability does not seem to correlate with the impact on cell viability. Indeed, after 24 h exposure, NDs were able to reduce B cell viability already starting from 50 μg mL^{-1}, while the same concentration did not induce any significant reduction of cell viability in monocytes, despite the higher internalization of NDs compared to lymphocytes. The lower cytotoxicity may be due to the phagocytic nature of monocytes, leading to a better processing and clearance of NDs. However, the lack of correlation may be due to the well-known sensitivity of B cells compared to other immune subpopulations, regardless of ND uptake.

This data highlights the ability of monocytes to internalize NDs and, together with the relatively low toxicity observed in this immune cell subpopulation, is in agreement with a recent study on innate immune effector cells showing the capacity of other kind of non-functionalized fluorescent NDs (FNDs), produced by the HTHP method, to be internalized without signs of toxicity by macrophages in a dose-dependent manner, displaying a greater uptake compared to NK cells [55].

Moreover, our findings are in line with a previous study reporting that monocytes are able to engulf other CBMs (*i.e.,* CNTs) in a more efficient manner compared to other immune cell populations [50]. However, the uptake of NDs is very limited compared to other carbon and non-carbon based materials [50,56–58], suggesting that NDs are able to escape the immune cells, including

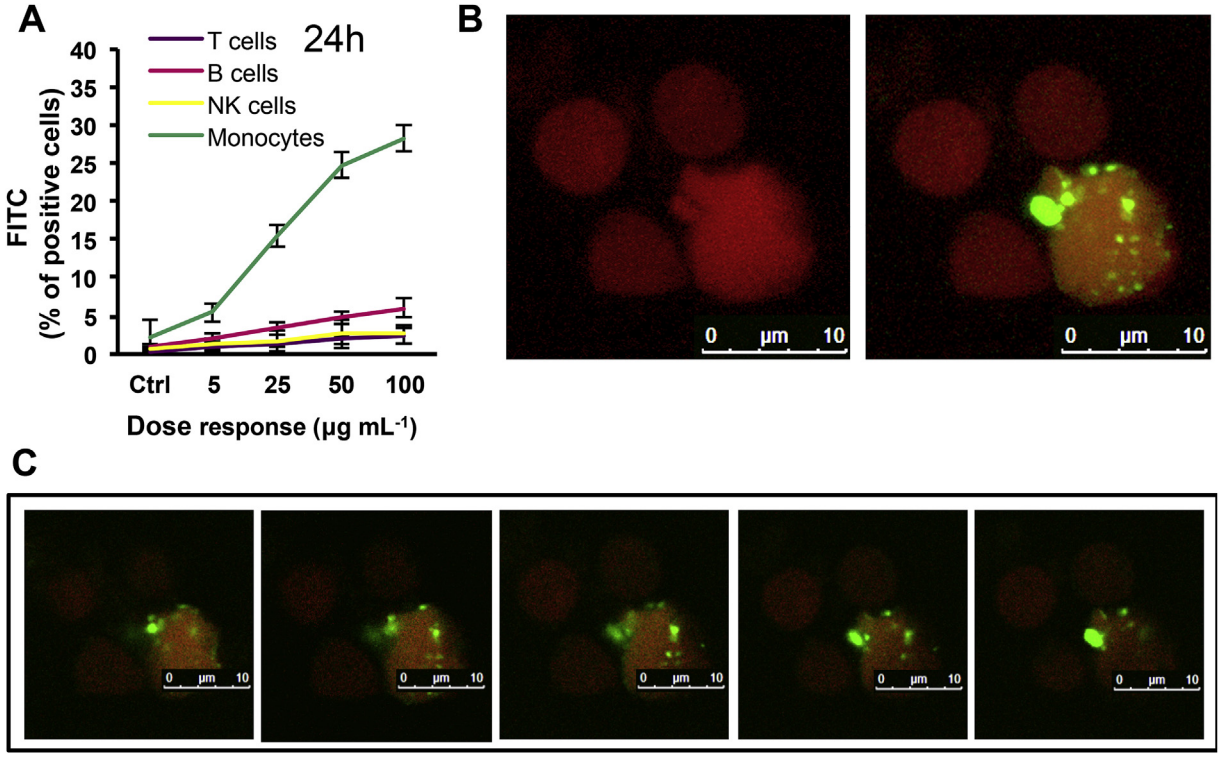

Fig. 5. Uptake of NDs-FITC by human PBMCs. (A) Internalization of increasing concentrations (5, 25, 50, and 100 μg mL^{-1}) of NDs-FITC into T cells, B cells, NK cells, and monocytes evaluated after 24 h exposure by flow cytometry; **(B)** Internalization evaluated by confocal microscopy after 24 h exposure to NDs-FITC (50 μg mL^{-1}). The red fluorescence of the propidium iodide stained cells (left panel) revealed the cell morphology, allowing to localize the NDs green fluorescence (right panel); **(C)** Consecutive slides from the top to the bottom of NDs-FITC internalization after 24 h incubation. (A colour version of this figure can be viewed online.)

monocytes (*e.g.,* after intravenous injection for medical applications) [59].

To demonstrate that our observations were due to an effective NDs internalization, and not simply to the adhesion of NDs to the cell surface, the intracellular location was confirmed by confocal microscopy analysis. As reported in previous studies for other CBMs, such as carbon nanotubes [50], cells were exposed to the intermediate concentration of 50 μg mL^{-1}, at the same time condition (24 h exposure) used for the flow cytometry analysis. To visualize the NDs intracellular distribution, cell morphology was identified by staining the cell cytoplasm with propidium iodide (PI), a fluorescent dye able to bind cell nuclear DNA and cytoplasmic RNAs [60]. Monocytes were identified by analyzing the cell morphology. Two dimensional projections of the fluorescence image stack, as well as cross-sectional composite images, were generated. As shown in Fig. 5B, the red fluorescence of the PI stained cells (left panel) revealed the cell morphology, allowing to localize the NDs green fluorescence (right panel). Additionally, serial sections from the top to the bottom of monocytes, acquired by confocal imaging, clearly confirmed that NDs-FITC were taken up into the cytoplasm of these cells (Fig. 5C).

The ability of monocytes to internalize NDs is likely due to their phagocytic capacity. Indeed, similarly to other nanoparticles, NDs are engulfed into the cell via endocytosis, as previously observed for other kind of human immune cells (*i.e.* human neutrophils and monocyte-derived dendritic cells) [61] and mammalian cells [62,63].

Thanks to this ability, Chu *et al.* demonstrated efficient plasmid DNA delivery by NDs in human liver carcinoma HepG2 cells, suggesting their use as an optimal vector easy to be internalized into the cells with a quick endosomal escape after endocytosis [63], while Pope *et al.* investigated the internalized NDs in living cells *in situ*, underlining the possibility to use NDs for drug-delivery application and as contrast agent tool *in vivo* [64].

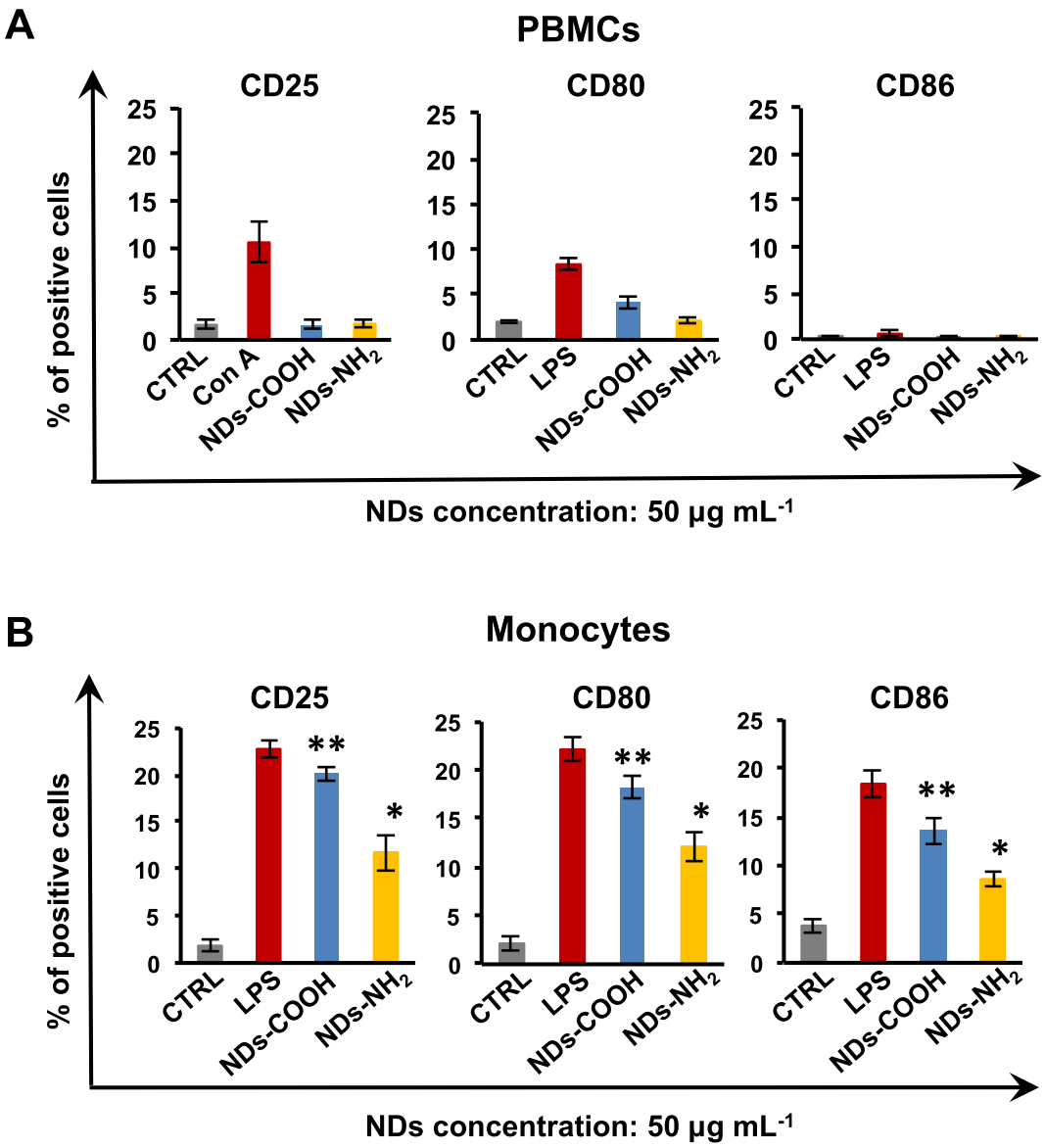

Fig. 6. Immune cell subpopulation activation. Cells were exposed to NDs-COOH or NDs-NH_2 (50 μg mL^{-1}) for 24 h and the effects on immune cell activation were evaluated. **(A)** Human PBMCs activation; **(B)** Human monocytes activation. The levels of a wide variety of activation markers (CD25, CD80, and CD86) were evaluated by flow cytometry. LPS or ConA were used as positive controls. Experiments were performed using cells from at least three different donors in triplicate. Statistical differences vs. negative controls (CTRL): *, $p < 0.05$; **, $p < 0.01$ (Student's t-test). (A colour version of this figure can be viewed online.)

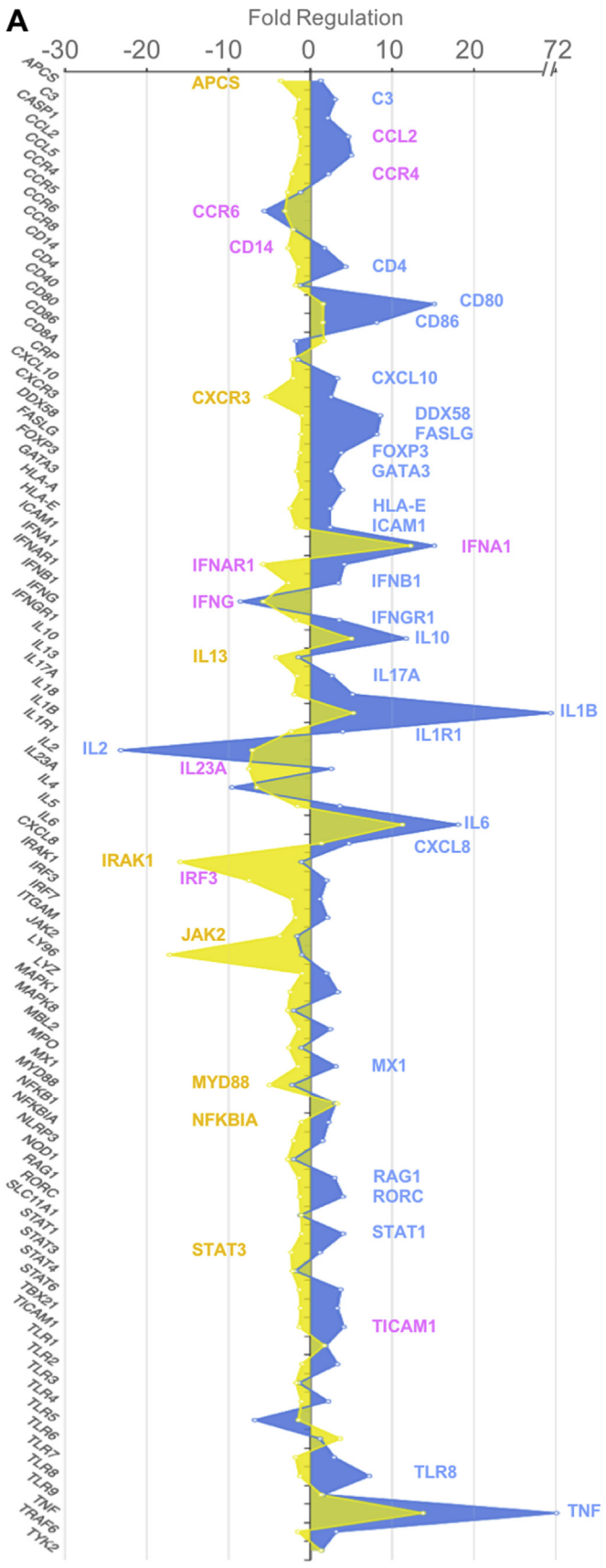

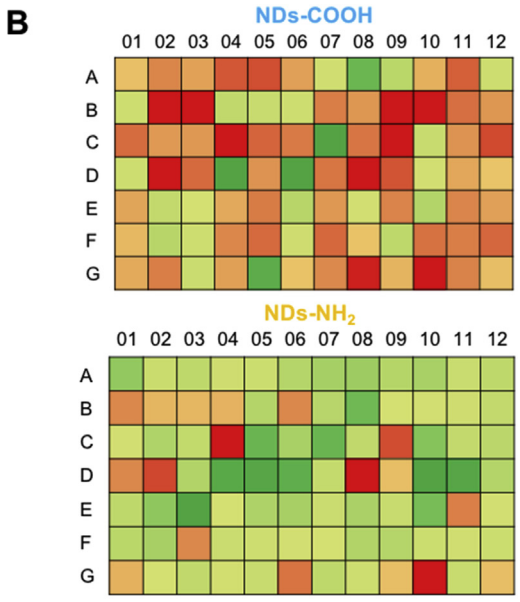

C

	Symbol	Fold Regulation NDs-COOH	Fold Regulation NDs-NH_2
$p < 0.05$ in both NDs	IFNA1	15,1	12,2
	CCL2	4,6	-1,2
	IFNAR1	4,1	-5,8
	TICAM1	4,0	-1,3
	IL23A	2,5	-7,5
	CCR4	2,2	-2,2
	IRF3	1,9	-7,5
	CD14	1,7	-2,7
	CCR6	-5,6	-3,1
	IFNG	-8,6	-5,8
$p < 0.05$ in NDs-COOH	TNF	72,6	13,7
	IL1B	29,3	5,2
	IL6	18,0	11,2
	CD80	15,1	1,5
	IL10	11,7	5,0
	DDX58	8,5	-1,0
	CD86	8,1	1,5
	FASLG	8,1	-1,1
	TLR8	7,2	-1,3
	CXCL8	4,7	1,3
	CD4	4,3	-1,5
	STAT1	4,0	-1,1
	RORC	3,9	-1,3
	IL1R1	3,9	-2,4
	FOXP3	3,8	-1,2
	IFNGR1	3,5	-1,8
	IFNB1	3,4	-2,7
	CXCL10	3,3	-2,1
	MX1	3,1	-1,5
	C3	3,0	-1,4
	RAG1	2,9	-1,4
	IL17A	2,6	-1,6
	GATA3	2,5	-1,6
	HLA-E	2,4	-2,4
	ICAM1	2,4	-1,7
	IL2	-23,2	-7,1
$p < 0.05$ in NDs-NH_2	CXCR3	2,5	-5,3
	NFKBIA	2,2	-1,1
	APCS	1,2	-3,6
	STAT3	1,1	-2,3
	IRAK1	-1,1	-15,9
	IL13	-1,5	-4,2
	JAK2	-1,6	-3,7
	MYD88	-2,3	-5,0

The obtained results are interesting for the possible development of biomedical applications exploiting monocyte-targeted nanoplatforms based on NDs for diagnostic and therapeutic applications addressing the new concept of "immunoengineering" [65]. Indeed, since monocytes are able to migrate to the site of tissue inflammation or infection, they can serve as vehicles to deliver several molecules, including contrast agents, drugs or genes, for a more specific and localized treatment. In addition, it has been reported that positively charged materials can increase the complexation ability with siRNA [66]. This observation, in addition to the higher biocompatibility showed by ND-NH_2, may facilitate their use for biomedical applications in this field. Moreover, we have previously suggested for other nanomaterials that the specific impact of monocytes can be exploited for monocyte-related diseases (*e.g.* for cancer treatment) [67]. Similarly, other studies have explored the NDs-induced stimulation of immune cells, including monocytes, as strategy to enhance anti-tumor activity [55].

3.5. Effects of functionality: changes in cell diameter and activation markers

To assess whether the NDs affect the functionality of the immune cells, we looked first at the diameter changes after treatment (Fig. S2). Hence, PBMCs were treated with the highest concentration of NDs-COOH or NDs-NH_2 not inducing a reduction of cell viability (50 μg mL^{-1}) for 6 and 24 h and the effect on cell activation was evaluated by changes in lymphocytes and monocytes cell diameter distribution by a Scepter Cell Counter.

Fig. S2 shows histograms representing diameter modifications of total PBMCs after treatment. NDs-COOH were able to induce monocyte activation already after 6 h exposure, as proved by the variation of monocyte fractions cell diameter compared to the negative control. The higher impact of NDs-COOH on human PBMCs compared to NDs-NH_2 was confirmed also increasing the exposure time up to 24 h. NDs-COOH treatment on PBMCs led to an increase in monocytes diameter, not observed for NDs-NH_2. Immune cells are able to change their diameter under activation stimuli by increasing the cellular volume. These findings demonstrate a role of NDs functionalization on their ability to induce immune activation of monocytes, suggesting that the amine-terminating chains on their surface provide a more biocompatible behavior on this immune cell population compared to the carboxylic group decoration.

To further investigate the effect of NDs-COOH and NDs-NH_2 on immune cell activation, a panel of specific cell surface differentiation markers was evaluated: the late activation marker CD25 (α-chain of the IL-2 receptor), and the co-stimulatory molecules CD80 and CD86. Human PBMCs were exposed to NDs-COOH or NDs-NH_2 (50 μg mL^{-1}) for 24 h and the expression of the selected surface differentiation markers was assessed by flow cytometry (Fig. 6A). Lipopolysaccharide (LPS; 2 μg mL^{-1}) was used as positive control. As observed in Fig. 6A, the materials did not exert any significant effect on PBMCs activation. However, after gating CD14+ cells, a high NDs-mediated cell activation was induced in monocytes (Fig. 6B). Both nanomaterials significantly increased the expression of CD25, CD80, and CD86 in monocytes with different potency, NDs-COOH ($p < 0.01$) being more active than NDs-NH_2 ($p < 0.05$). In conclusion, the obtained results show that the different NDs surface functionalization seems to have a role in the ability of NDs to influence monocyte activation, highlighting the reduced immune impact conferred by the amino-functionalization, probably thanks also to a decrease aggregation of the NDs themselves. These observations confirm the cell diameter results previously described (Fig. S2) and are in agreement with a recent study on innate immune effector cells, showing cell activation after exposure to FNDs [55,68]. Moreover, the different modulation played by the functionalization here observed is in line with findings concerning other nanomaterials reporting that the amino- and carboxylic acid-decoration shifted macrophages to an anti-inflammatory M2 and inflammatory M1 phenotype, respectively [69].

3.6. Gene expression impact

Considering that the immune system works by switching genes on and off, the understanding of nanomaterial-immune system interaction cannot overlook the genomic level. Therefore, we used a molecular strategy to characterize *ex vivo* the impact of NDs on immune cells, as we previously reported for GO [39]. To the best of our knowledge, there are no reports on gene expression impact of different NDs on human immune cells. In the present study, to evaluate the possible effect of different functionalized NDs on key pathways controlling innate and adaptive immune response, cells were exposed to NDs-COOH or NDs-NH_2 (50 μg mL^{-1}) for 24 h and gene expression analysis of 84 highly selected immune genes was carried out (Fig. 7). Fig. 7A shows the expression ratio of NDs-treated versus control samples for all the considered genes after treatment with NDs-COOH or NDs-NH_2, also displayed in Fig. 7B as heat map showing individual genes of the plot colored according to their standardized expression values (green squares = down-regulated genes, yellow square = unmodulated genes, red squares = up-regulated genes). The values of fold change and fold regulation with corresponding *p*-value for the examined genes in the gene expression analysis reported in Fig. 7 are described in Table S1 and Table S2, respectively.

The gene expression analysis clearly revealed the divergent immune modulation induced by the two types of NDs. Overall, NDs-COOH not only evoked a wider and more pronounced regulation of immune-modulatory transcripts, but also induced an opposite effect on their expression trend as compared to NDs-NH_2 (Fig. 7A–B). In fact, the number of transcripts significantly modulated ($p < 0.05$) by NDs-COOH was twice as high as the ones altered by NDs-NH_2 (Fig. 7C). The large majority of transcripts displayed an opposite directionality between the two materials. In particular, NDs-NH_2 had a limited impact on the expression of central inflammation-related transcripts, overall exerting an inhibitory or neutral effect. NDs-NH_2 modulation was restricted to genes encoding for pro-inflammatory, monocyte-related, cytokines such as *IL1B*, *TNF*, and *IL6*, resulting in a coherent, although non-statistically significant up-regulation. Such an effect was much more pronounced in the case of NDs-COOH, which was sustained by *STAT3* induction [70], possibly triggering the up-regulation of *IL-10*, a pleiotropic cytokine with both pro and anti-inflammatory proprieties [71].

Moreover, NDs-COOH also induced the expression of the

Fig. 7. Immune gene expression. (A) Fold regulation variation of the analyzed immune genes, compared to the control, after exposure of PBMCs to 50 μg mL^{-1} of NDs-COOH or NDs-NH_2 for 24 h. Significantly up-regulated or down-regulated genes ($p < 0.05$) are reported in the graph (pink = $p < 0.05$ in both NDs, blue = $p < 0.05$ in NDs-COOH, and green = $p < 0.05$ in NDs-NH_2). Samples that did not satisfy the quality control (indicated as N/A in Table S1) were not considered. Table S1 indicates the gene of correspondence for A to G and 01 to 12. **(B)** Heat-map showing individual genes colored according to their standardized expression values (green squares = fold regulation < −8, yellow square = unmodulated fold regulation, red squares = fold regulation > 8). **(C)** Table displaying the Fold Regulation of significantly up-regulated or down-regulated genes ($p < 0.05$): green squares = Fold Regulation < −8, yellow squares = unmodulated fold regulation, red squares = Fold Regulation > 8 (pink = $p < 0.05$ in both NDs, blue = $p < 0.05$ in NDs-COOH, and green = $p < 0.05$ in NDs-NH_2). (A colour version of this figure can be viewed online.)

activation markers CD80 and CD86 (constitutionally expressed by B cells and monocytes, respectively), and chemokine receptors such as CCR6, expressed prevalently by B cell. This modulation is paired with the up-regulation of Toll-like-receptor related transcripts (*TLR8* and *TICAM1*), adhesion markers (*ICAM1*) and lineage markers such as *CD4* (expressed by both T cell and monocytes) and *CD14* (expressed by monocytes). These findings are consistent with a prominent activation of monocyte/antigen presenting cells functions [72,73].

This response is likely linked to the ability of monocytes and, at lesser extent, of B cells to internalize different nanomaterials, which could ultimately lead to their non-specific activation.

Indeed, other studies reported a significant impact on monocytes/macrophages observed for FNDs, which were able to be taken up by monocytes and induce their activation [55], as well as for other CBMs such as graphene-based materials [74], highlighting their efficient engulfment into primary human monocyte-derived macrophages without signs of toxicity [75] and the ability to promote a pro-inflammatory polarization of macrophages [76]. Similarly, we have recently reported the activation of monocytes induced by GO as a promising strategy to improve bone regeneration [77]. However, the putative mechanism underlying the uptake of NDs into monocyte and their activation still needs further clarification. In this view, previous studies carried out on other cell models suggested that NDs can be internalized via phagocytosis or through direct diffusion across the cell membrane [62], highlighting a mechanism involving clathrin-dependent endocytotic process [78,79].

However, the differential induction of inflammatory signaling between the two nanomaterials suggests the perturbations of different molecular mechanisms. For instance, NDs-NH_2 down-regulated the expression of genes such as *MyD88*, which plays a critical role in the control of innate immune responses and inflammation through the modulation of Toll-like receptor (TLR) and IL-1 receptor (IL1R) family signaling [80], and *IRAK1*, requiring the interaction with MyD88 for its activation. *NFKBIA* down-regulation might partially explains the attenuated induction of *IL-6* in NDs-NH_2 treated cells.

NDs-COOH induced a strong modulation of the interferon signaling, which bridges innate and adaptive immune compartments. NDs-COOH effects are consistent with an activation of the type-I interferon signaling (*i.e.* Interferon α and β) as substantiated by the concomitant induction of *IFNA1*, *IFNB1*, and *STAT1*, followed by a homeostatic down-regulation of the cognate receptor *IFNAR1* [81] as putative compensatory mechanism. A less coherent up-regulation of the type-I interferon signaling was observed in the case of NDs-NH_2 where only *IFNA1* was significantly modulated.

Remarkably, NDs-COOH (and not NDs-NH_2) specifically inflected the signaling involved in T-cell lineage differentiation, which was heavily skewed toward a T helper 2 (Th2) and T helper 17 (Th17) polarization. This process is demonstrated by the up-regulation of *GATA3*, a transcriptional factor central in Th2 differentiation, and *RORC*, which, acting downstream IL-6 signaling, dictates Th17 lineage commitment, together with *IL1B* and *IL23* [82] (up-regulated following NDs-COOH challenge). The modulation of Th17 differentiation is also substantiated by the up-regulation of *IL17A*, a landmark feature of Th17 cells [83], which triggers the up-regulation of the CXCL8 chemokine. The induction of a Th2 and Th17 polarization is reinforced by the concomitant inhibition of classic T-helper 1 (Th1) transcripts such as *IFNG* and *IL2*, which were down-regulated after NDs-COOH treatment. *FOXP3* was up-regulated by ND-COOH. Although stable expression of FOXP3 in mice is a characteristic of T-regulatory cells (T-reg), in humans it is transiently expressed by a high proportion of T cell upon activation [84]. T cell activation by NDs-COOH is also supported by the up-regulation of *FASLG*, *CXCL10* and its receptor *CXCR3*. The effect exerted by NDs-COOH on the signaling involved in T cell lineage differentiation could be of interest for possible biomedical application, like in immunization implementation research for vaccines. An opposite effect on Th2 and Th17 polarization was induced by NDs-NH_2, which significantly down-regulated *IL13*, a classic Th2 cytokine, while suppression of Th1 signaling (down-regulation of *IFNG*, *IL2*, and *JAK2*) was shared between the two materials.

3.7. Protein level impact: cytokines release

Finally, to evaluate the effects of NDs-COOH and NDs-NH_2 at the protein level on human immune cells, a panel of 7 different cytokines was quantified by multiplex Enzyme-Linked Immunosorbent Assay (ELISA): interleukin (IL)-2, interferon (IFN)-γ, IL-4, IL-6, IL-10 IL-1β, and tumor necrosis factor (TNF)-α.

As shown in Fig. 8A, NDs-COOH and NDs-NH_2 did not induce any significant release of IL-2, IFN-γ, and IL-4 from human immune cells. On the contrary, a significant increase of IL-1β and IL-10 was induced by NDs-COOH (p-value < 0.01) and NDs-NH_2 (p-value < 0.05) with different statistical significance, NDs-COOH exerting a more prominent response (Fig. 8B). A significant release (p-value < 0.05) of IL-6 and TNF-α was also observed for both nanomaterials.

While the exposure of PBMCs to NDs did not induce the release of Th1 (IL-2 and IFN-γ) and Th2 (IL-4) cytokine production, the enhanced secretion observed for TNFα, IL-1β, IL-6, and IL-10, all key players of the innate immune system response, demonstrates that the action of NDs is directed to the activation of the acute inflammatory process. Indeed, TNFα is a potent pyrogenic cytokine normally secreted by monocytes/macrophages in response to a pathogen infection [85]. TNFα main functions are vasodilation and loss of vascular permeability, which promote lymphocyte, neutrophil, and monocyte infiltration. It helps to recruit these cells to the inflammation site by regulating chemokine release such as CCL5 and CXCL8 [86], also induced by NDs-COOH. Similarly to TNFα, IL-1β is also an endogenous pyrogen that is produced and released at the early stages of the immune response to infections, lesions, and stress [87]. During inflammation, IL1β stimulates the central nervous system to induce fever and prostaglandin secretion acting also as chemoattractant for T cells and granulocytes. IL-1β production and secretion requires assembly of the inflammasome, a cytoplasmic complex containing several proteins that serves as a molecular platform for activation of the cysteine protease caspase [87]. Similar functions are exerted by IL-6, being as well an endogenous pyrogen. IL-6 main function leads to recruitment of other monocytes to the inflammation site, while blocking the recruitment of anti-inflammatory T cells, Tregs, to the site of infection [88]. On the other hand, IL-10 plays a crucial role in controlling the immune cell response [89], being a pleiotropic cytokine with both pro and anti-inflammatory proprieties [71].

Overall, these findings are consistent with the trend previously observed for gene expression analysis of these inflammatory mediators. In particular, the lack of effect on the release of IL-2 and IFN-γ is in line with the suppression of Th1 signaling induced by the two NDs at the gene level, while the enhanced secretion observed for TNF-α, IL-1β, IL-6, and IL-10, overall more pronounced for NDs-COOH, is consistent with the upregulated expression of these cytokines induced by NDs-COOH. The obtained findings support the ability of NDs, and in particular NDs-COOH, to promote the activation of monocytes and acute inflammatory process, as evidenced by the enhanced secretion of pro-inflammatory, monocyte-related, cytokines. Moreover, our findings are in line with our previous studies showing that the presence of the amine groups reduce the impact of other CBMs on immune cells also in terms of cytokines

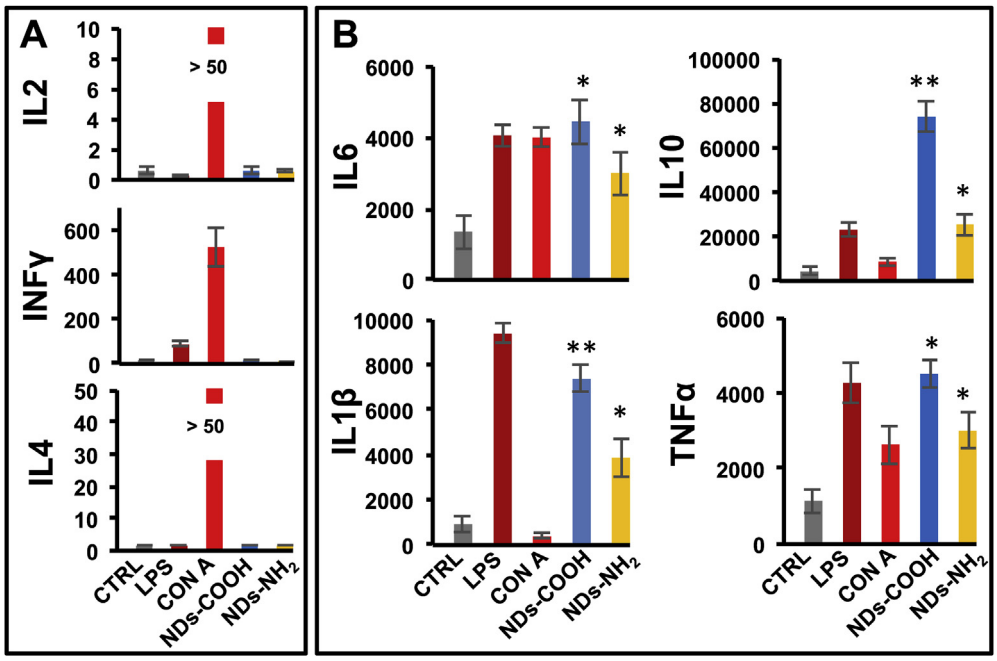

Fig. 8. Cytokine secretion. Cytokine secretion was analyzed by multiplex ELISA after 24 h exposure of PBMCs to NDs-COOH or NDs-NH_2 (50 μg mL^{-1}). Untreated PBMCs were used as negative controls (CTRL); ConA (10 μg mL^{-1}) or LPS (2 μg mL^{-1}) were used as positive controls. Cytokines of the adaptive response **(A)** and the innate response were assessed **(B)**. Cytokine secretion values are expressed in pg mL^{-1}. Statistical significance difference of untreated samples versus NDs treated samples was calculated by Student's t-test (*, $p < 0.05$; **, $p < 0.01$). (A colour version of this figure can be viewed online.)

release. For example, we have previously demonstrated that amino functionalization of graphene oxide inhibits the secretion of several inflammatory mediators such as IL-6 and TNF-α [51]. Of note, a very recent study on the impact of amino- and carboxylic acid-decorated NDs on a human macrophage cell line (*i.e.*, PLB-985 cells) did not observe any secretion of TNF-α after 24 h exposure to 25 μg mL^{-1}, while we here highlight that increasing the concentration up to 50 μg mL^{-1} can induce the release of this critical pro-inflammatory mediator [19].

4. Conclusions

The elucidation of the potential immune impact of NDs represents a critical step to ensure their safe use for biomedical applications. Therefore, in the present study we performed an integrative characterization of the impact of two differently functionalized NDs on human primary immune blood cell subpopulations, as a model which closely mimic the *in vivo* scenario of first interactions between intravenously injected biomedical nanotools and the immune system.

After confirming the high hemocompatibility of NDs, their effects were evaluated on different immune cell subpopulations (B cells, T cells, NK cells, and monocytes), revealing that carboxylated NDs, but not amino functionalized NDs, induced a slight reduction of cell viability, affecting in particular monocytes and, to a lesser extent, B cells. Moreover, to deeper characterize the immune impact of NDs, their immunologic effects were depicted through gene expression and protein analysis, revealing that, despite their low cytotoxicity, NDs were able to elicit pro-inflammatory responses and signs of immune cell activation with different potency depending on their functionalization, COOH-modified NDs showing more prominent responses, particularly relevant for IFN-I signaling, Th2 and Th17 polarization, and in monocytes. Notably, monocytes showed the ability to selectively internalize NDs, not displayed by the other immune cell subpopulations. This observation, together with the enhanced biocompatibility conferred by the amino-functionalization in terms of toxicity and functionality (assessed at the protein and gene level) may potentially be exploited for the development of monocyte-targeted nanoplatforms based on NDs for diagnostic and therapeutic applications. In this view, the results of this study represent a significant step forward in the understanding of the immune-compatibility of NDs and the role of surface functionalization on their impact at the immune level for the development of future tools in biomedicine.

In conclusion, we here provided new information on the hemato- and immunocompatibility of nanodiamonds and, similarly to our previous observations on carbon nanotubes and graphene [39,40], we have demonstrated that even if both NDs have shown a proinflammatory action, NH_2 modification appears to mitigate these responses. However, considering the immune response activated by the NDs, further studies on the bio- and the *in vivo* immune compatibility are required before these materials can be translated into the clinic. Our data provide new information on the role of the amino-functionalization impact of NDs, paving the way for further pre-clinical studies aimed at the developing ND-based future medical tools.

Declaration of competing interest

The authors declare that they have no known competing financial interests or personal relationships that could have appeared to influence the work reported in this paper.

Acknowledgements

The authors thank the European Union HORIZON 2020 Research and Innovation Programme under MSCA RISE 2016 project Carbo-Immap grant (n. 734381).

Appendix A. Supplementary data

Supplementary data to this article can be found online at https://doi.org/10.1016/j.carbon.2020.01.003.

References

[1] S. Das, S. Mitra, S.M.P. Khurana, N. Debnath, Nanomaterials for biomedical applications, Front. Life Sci. 7 (3–4) (2013) 90–98.
[2] F.C. Adams, C. Barbante Nanoscience, Nanotechnology and spectrometry, Spectrochim. Acta B 86 (2013) 3–13.
[3] L. Delogu, G. Vidili, E. Venturelli, C. Ménard-Moyon, M. Zoroddu, G. Pilo, et al., Functionalized multiwalled carbon nanotubes as ultrasound contrast agents, Proc. Natl. Acad. Sci. 109 (41) (2012) 16612–16617.
[4] M.E. Godsey, S. Suryaprakash, K.W. Leong, Materials innovation for co-delivery of diverse therapeutic cargos, RSC Adv. 3 (47) (2013) 24794–24811.
[5] C. Wang, J. Li, C. Amatore, Y. Chen, H. Jiang, X.M. Wang, Gold nanoclusters and graphene nanocomposites for drug delivery and imaging of cancer cells, Angew. Chem. Int. Ed. 50 (49) (2011) 11644–11648.
[6] M. Orecchioni, C. Menard-Moyon, L.G. Delogu, A. Bianco, Graphene and the immune system: challenges and potentiality, Adv. Drug Deliv. Rev. 105B (2016) 163–175.
[7] X.Y. Zhang, W.B. Hu, J. Li, L. Tao, Y. Wei, A comparative study of cellular uptake and cytotoxicity of multi-walled carbon nanotubes, graphene oxide, and nanodiamond, Toxicol Res-Uk 1 (1) (2012) 62–68.
[8] A.M. Schrand, L. Dai, J.J. Schlager, S.M. Hussain, E. Osawa, Differential biocompatibility of carbon nanotubes and nanodiamonds, Diam. Relat. Mater. 16 (12) (2007) 2118–2123.
[9] K.-K. Liu, C.-L. Cheng, C.-C. Chang, J.-I. Chao, Biocompatible and detectable carboxylated nanodiamond on human cell, Nanotechnology 18 (32) (2007) 325102.
[10] A.M. Schrand, H. Huang, C. Carlson, J.J. Schlager, E. Omacr Sawa, S.M. Hussain, et al., Are diamond nanoparticles cytotoxic? J. Phys. Chem. B 111 (1) (2007) 2–7.
[11] D.E.J. Waddington, T. Boele, E. Rej, D.R. McCamey, N.J.C. King, T. Gaebel, et al., Phase-encoded hyperpolarized nanodiamond for magnetic resonance imaging, Sci. Rep. 9 (1) (2019) art. no. 5950.
[12] A.I. Shames, A.M. Panich, in: J.-C. Arnault (Ed.), Paramagnetic Defects in Nanodiamonds *in* Nanodiamonds - Advanced Material Analysis, Properties and Applications, Elsevier, 2017, pp. 131–154.
[13] G. Balasubramanian, I.Y. Chan, R. Kolesov, M. Al-Hmoud, J. Tisler, C. Shin, et al., Nanoscale imaging magnetometry with diamond spins under ambient conditions, Nature 455 (7213) (2008) 648–651.
[14] V.N. Mochalin, O. Shenderova, D. Ho, Y. Gogotsi, The properties and applications of nanodiamonds, Nat. Nanotechnol. 7 (1) (2011) 11–23.
[15] D. Ho, C.H. Wang, E.K. Chow, Nanodiamonds: the intersection of nanotechnology, drug development, and personalized medicine, Sci. Adv. 1 (7) (2015), e1500439.
[16] K. van der Laan, M. Hasani, T. Zheng, R. Schirhagl, Nanodiamonds for *in vivo* applications, Small 14 (19) (2018), e1703838.
[17] K.P. Loh, D. Ho, G.N.C. Chiu, D.T. Leong, G. Pastorin, E.K. Chow, Clinical applications of carbon nanomaterials in diagnostics and therapy, Adv. Mater. 30 (47) (2018), e1802368.
[18] A. Sigaeva, A. Morita, S.R. Hemelaar, R. Schirhagl, Nanodiamond uptake in colon cancer cells: the influence of direction and trypsin-EDTA treatment, Nanoscale 11 (37) (2019) 17357–17367.
[19] V.S. Madamsetty, A. Sharma, M. Toma, S. Samaniego, A. Gallud, E. Wang, et al., Tumor selective uptake of drug-nanodiamond complexes improves therapeutic outcome in pancreatic cancer, Nanomedicine 18 (2019) 112–121.
[20] Z. Chen, C. Wang, T.F. Li, K. Li, Y. Yue, X. Liu, et al., Doxorubicin conjugated with nanodiamonds and in free form commit glioblastoma cells to heterodromous fates, Nanomedicine 14 (3) (2019) 335–351.
[21] B. Woodhams, L. Ansel-Bollepalli, J. Surmacki, H. Knowles, L. Maggini, M. de Volder, et al., Graphitic and oxidised high pressure high temperature (HPHT) nanodiamonds induce differential biological responses in breast cancer cell lines, Nanoscale 10 (25) (2018) 12169–12179.
[22] M.D. Torelli, N.A. Nunn, O.A. Shenderova, A perspective on fluorescent nanodiamond bioimaging, Small 15 (2019), e1902151.
[23] R. Eivazzadeh-Keihan, A. Maleki, M. de la Guardia, M.S. Bani, K.K. Chenab, P. Pashazadeh-Panahi, et al., Carbon based nanomaterials for tissue engineering of bone: building new bone on small black scaffolds: a review, J. Adv. Res. 18 (2019) 185–201.
[24] D. Passeri, F. Rinaldi, C. Ingallina, M. Carafa, M. Rossi, M.L. Terranova, et al., Biomedical applications of nanodiamonds: an overview, J. Nanosci. Nanotechnol. 15 (2) (2015) 972–988.
[25] X.Q. Zhang, R. Lam, X. Xu, E.K. Chow, H.J. Kim, D. Ho, Multimodal nanodiamond drug delivery carriers for selective targeting, imaging, and enhanced chemotherapeutic efficacy, Adv. Mater. 23 (41) (2011) 4770–4775.
[26] X.Q. Zhang, M. Chen, R. Lam, X. Xu, E. Osawa, D. Ho, Polymer-functionalized nanodiamond platforms as vehicles for gene delivery, ACS Nano 3 (9) (2009) 2609–2616.
[27] L.W. Tsai, Y.C. Lin, E. Perevedentseva, A. Lugovtsov, A. Priezzhev, C.L. Cheng, Nanodiamonds for medical applications: interaction with blood *in vitro* and *in vivo*, Int. J. Mol. Sci. 17 (7) (2016) 1111.
[28] V.A. Shkurupy, S.A. Arkhipov, D.V. Neshchadim, E.S. Akhramenko, A.V. Troitskii, *In vitro* effects of nanosized diamond particles on macrophages, Bull. Exp. Biol. Med. 158 (4) (2015) 500–503.
[29] A.E. Pentecost, C.E. Witherel, Y. Gogotsi, K.L. Spiller, Anti-inflammatory effects of octadecylamine-functionalized nanodiamond on primary human macrophages, Biomater. Sci. 5 (10) (2017) 2131–2143.
[30] H. Zhang, L. Zhang, Z. Li, Q. Wu, J. Gao, *In vitro* immune activation of Raw264.7 cells by nanodiamonds with different surface chemistry, J. Nanosci. Nanotechnol. 18 (2) (2018) 815–822.
[31] O.A. Williams, M. Nesladek, M. Daenen, S. Michaelson, A. Hoffman, E. Osawa, et al., Growth, electronic properties and applications of nanodiamond, Diam. Relat. Mater. 17 (7) (2008) 1080–1088.
[32] Z. Wang, C. Xu, C. Liu, Surface modification and intrinsic green fluorescence emission of a detonation nanodiamond, J. Mater. Chem. C 1 (40) (2013) 6630–6636.
[33] A.R. Kirmani, W. Peng, R. Mahfouz, A. Amassian, Y. Losovyj, H. Idriss, et al., On the relation between chemical composition and optical properties of detonation nanodiamonds, Carbon 94 (2015) 79–84.
[34] A.M. Vervald, S.A. Burikov, O.A. Shenderova, N. Nunn, D.O. Podkopaev, I.I. Vlasov, et al., Relationship between fluorescent and vibronic properties of detonation nanodiamonds and strength of hydrogen bonds in suspensions, J. Phys. Chem. C 120 (34) (2016) 19375–19383.
[35] V.N. Mochalin, Y. Gogotsi, Wet chemistry route to hydrophobic blue fluorescent nanodiamond, J. Am. Chem. Soc. 131 (13) (2009) 4594–4595.
[36] A. Krueger, The structure and reactivity of nanoscale diamond, J. Mater. Chem. 18 (13) (2008) 1485–1492.
[37] I.I. Kulakova, Surface chemistry of nanodiamonds, Phys. Solid State 46 (4) (2004) 636–643.
[38] M. Dubois, K. Guerin, N. Batisse, E. Petit, A. Hamwi, N. Komatsu, et al., Solid state NMR study of nanodiamond surface chemistry, Solid State Nucl. Magn. Reson. 40 (4) (2011) 144–154.
[39] M. Orecchioni, D.A. Jasim, M. Pescatori, R. Manetti, C. Fozza, F. Sgarrella, et al., Molecular and genomic impact of large and small lateral dimension graphene oxide sheets on human immune cells from healthy donors, Adv. Healthc. Mater. 5 (2) (2016), 276-2.
[40] M. Pescatori, D. Bedognetti, E. Venturelli, C. Menard-Moyon, C. Bernardini, E. Muresu, et al., Functionalized carbon nanotubes as immunomodulator systems, Biomaterials 34 (18) (2013) 4395–4403.
[41] H. Huang, E. Pierstorff, E. Osawa, D. Ho, Active nanodiamond hydrogels for chemotherapeutic delivery, Nano Lett. 7 (11) (2007) 3305–3314.
[42] K. Mitura, M. Jedrzejewska-Szczerska, P. Ceynowa, M. Dudek, M. Cicha, I. Kotela, et al., Haemocompatibility of non-functionalized and plasmachemical functionalized detonation nanodiamond particles, Arch. Metall. Mater. 60 (3) (2015) 2183–2189.
[43] K.H. Liao, Y.S. Lin, C.W. Macosko, C.L. Haynes, Cytotoxicity of graphene oxide and graphene in human erythrocytes and skin fibroblasts, ACS Appl. Mater. Interfaces 3 (7) (2011) 2607–2615.
[44] I. Schmid, C. Uittenbogaart, B.D. Jamieson, Live-cell assay for detection of apoptosis by dual-laser flow cytometry using Hoechst 33342 and 7-amino-actinomycin D, Nat. Protoc. 2 (1) (2007) 187–190.
[45] K. Bhattacharya, S.P. Mukherjee, A. Gallud, S.C. Burkert, S. Bistarelli, S. Bellucci, et al., Biological interactions of carbon-based nanomaterials: from coronation to degradation, Nanomedicine 12 (2) (2016) 333–351.
[46] D.R. Hristov, L. Rocks, P.M. Kelly, S.S. Thomas, A.S. Pitek, P. Verderio, et al., Tuning of nanoparticle biological functionality through controlled surface chemistry and characterisation at the bioconjugated nanoparticle surface, Sci. Rep. 5 (2015) art. no. 17040.
[47] E. Frohlich, The role of surface charge in cellular uptake and cytotoxicity of medical nanoparticles, Int. J. Nanomed. 7 (2012) 5577–5591.
[48] M. Lundqvist, J. Stigler, G. Elia, I. Lynch, T. Cedervall, K.A. Dawson, Nanoparticle size and surface properties determine the protein corona with possible implications for biological impacts, Proc. Natl. Acad. Sci. USA 105 (38) (2008) 14265–14270.
[49] M. Aramesh, O. Shimoni, K. Ostrikov, S. Prawer, J. Cervenka, Surface charge effects in protein adsorption on nanodiamonds, Nanoscale 7 (13) (2015) 5726–5736.
[50] L.G. Delogu, E. Venturelli, R. Manetti, G.A. Pinna, C. Carru, R. Madeddu, et al., *Ex vivo* impact of functionalized carbon nanotubes on human immune cells, Nanomedicine 7 (2) (2012) 231–243.
[51] M. Orecchioni, D. Bedognetti, L. Newman, C. Fuoco, F. Spada, W. Hendrickx, et al., Single-cell mass cytometry and transcriptome profiling reveal the impact of graphene on human immune cells, Nat. Commun. 8 (1) (2017) 1109.
[52] B. Fadeel, Hide and seek: nanomaterial interactions with the immune system, Front. Immunol. 10 (2019) 133.
[53] Y.A. Huang, C.W. Kao, K.K. Liu, H.S. Huang, M.H. Chiang, C.R. Soo, et al., The effect of fluorescent nanodiamonds on neuronal survival and morphogenesis, Sci. Rep. 4 (2014) 6919.
[54] L.P. McGuinness, Y. Yan, A. Stacey, D.A. Simpson, L.T. Hall, D. Maclaurin, et al., Quantum measurement and orientation tracking of fluorescent nanodiamonds inside living cells, Nat. Nanotechnol. 6 (6) (2011) 358–363.
[55] L.P. Suarez-Kelly, A.R. Campbell, I.V. Rampersaud, A. Bumb, M.S. Wang, J.P. Butchar, et al., Fluorescent nanodiamonds engage innate immune effector cells: a potential vehicle for targeted anti-tumor immunotherapy, Nanomedicine 13 (3) (2017) 909–920.

[56] L.G. Delogu, A. Magrini, A. Bergamaschi, N. Rosato, M.I. Dawson, N. Bottini, et al., Conjugation of antisense oligonucleotides to PEGylated carbon nanotubes enables efficient knockdown of PTPN22 in T lymphocytes, Bioconjug. Chem. 20 (3) (2009) 427–431.
[57] C. Farace, P. Sanchez-Moreno, M. Orecchioni, R. Manetti, F. Sgarrella, Y. Asara, et al., Immune cell impact of three differently coated lipid nanocapsules: pluronic, chitosan and polyethylene glycol, Sci. Rep. 6 (2016) 18423.
[58] G. Reina, A. Ruiz, D. Murera, Y. Nishina, A. Bianco, "Ultramixing": a simple and effective method to obtain controlled and stable dispersions of graphene oxide in cell culture media, ACS Appl. Mater. Interfaces 11 (8) (2019) 7695–7702.
[59] H. Jin, D.A. Heller, R. Sharma, M.S. Strano, Size-dependent cellular uptake and expulsion of single-walled carbon nanotubes: single particle tracking and a generic uptake model for nanoparticles, ACS Nano 3 (1) (2009) 149–158.
[60] T. Suzuki, K. Fujikura, T. Higashiyama, K. Takata, DNA staining for fluorescence and laser confocal microscopy, J. Histochem. Cytochem. 45 (1) (1997) 49–53.
[61] A.V. Karpukhin, N.V. Avkhacheva, R.Y. Yakovlev, Kulakova II, V.A. Yashin, G.V. Lisichkin, et al., Effect of detonation nanodiamonds on phagocyte activity, Cell Biol. Int. 35 (7) (2011) 727–733.
[62] O. Faklaris, V. Joshi, T. Irinopoulou, P. Tauc, M. Sennour, H. Girard, et al., Photoluminescent diamond nanoparticles for cell labeling: study of the uptake mechanism in mammalian cells, ACS Nano 3 (12) (2009) 3955–3962.
[63] Z. Chu, K. Miu, P. Lung, S. Zhang, S. Zhao, H.C. Chang, et al., Rapid endosomal escape of prickly nanodiamonds: implications for gene delivery, Sci. Rep. 5 (2015) 11661.
[64] I. Pope, L. Payne, G. Zoriniants, E. Thomas, O. Williams, P. Watson, et al., Coherent anti-Stokes Ramant scattering microscopy of single nanodiamonds, Nat. Nanotechnol. 9 (11) (2014) 940–946.
[65] M.S. Goldberg Immunoengineering, How nanotechnology can enhance cancer immunotherapy, Cell 161 (2) (2015) 201–204.
[66] A. Schroeder, C.G. Levins, C. Cortez, R. Langer, D.G. Anderson, Lipid-based nanotherapeutics for siRNA delivery, J. Intern. Med. 267 (1) (2010) 9–21.
[67] J. Russier, V. Leon, M. Orecchioni, E. Hirata, P. Virdis, C. Fozza, et al., Few-layer graphene kills selectively tumor cells from myelomonocytic leukemia patients, Angew Chem. Int. Ed. Engl. 56 (11) (2017) 3014–3019.
[68] K.A. Abbas, A.H. Lichtman, S. Pillai, D.L. Baker, A. Baker, Cellular Molecular Immunology, ninth ed., Elsevier, 2018.
[69] M. Bartneck, H.A. Keul, S. Singh, K. Czaja, J. Bornemann, M. Bockstaller, et al., Rapid uptake of gold nanorods by primary human blood phagocytes and immunomodulatory effects of surface chemistry, ACS Nano 4 (6) (2010) 3073–3086.
[70] L. Lu, F. Zhu, M. Zhang, Y. Li, A.C. Drennan, S. Kimpara, et al., Gene regulation and suppression of type I interferon signaling by STAT3 in diffuse large B cell lymphoma, Proc. Natl. Acad. Sci. USA 115 (3) (2018) E498–E505.
[71] S. Mocellin, M.C. Panelli, E. Wang, D. Nagorsen, F.M. Marincola, The dual role of IL-10, Trends Immunol. 24 (1) (2003) 36–43.
[72] E.A. Ivanova, A.N. Orekhov, Monocyte activation in immunopathology: cellular test for development of diagnostics and therapy, J. Immunol. Res. 2016 (2016) 4789279.
[73] J. Fleischer, E. Soeth, N. Reiling, E. Grage-Griebenow, H.D. Flad, M. Ernst, Differential expression and function of CD80 (B7-1) and CD86 (B7-2) on human peripheral blood monocytes, Immunology 89 (4) (1996) 592–598.
[74] S.A. Sydlik, S. Jhunjhunwala, M.J. Webber, D.G. Anderson, R. Langer, *In vivo* compatibility of graphene oxide with differing oxidation states, ACS Nano 9 (4) (2015) 3866–3874.
[75] S.P. Mukherjee, M. Bottini, B. Fadeel, Graphene and the immune system: a romance of many dimensions, Front. Immunol. 8 (2017) 673.
[76] J. Ma, R. Liu, X. Wang, Q. Liu, Y. Chen, R.P. Valle, et al., Crucial role of lateral size for graphene oxide in activating macrophages and stimulating pro-inflammatory responses in cells and animals, ACS Nano 9 (10) (2015) 10498–10515.
[77] V. Bordoni, G. Reina, M. Orecchioni, G. Furesi, S. Thiele, C. Gardin, et al., Stimulation of bone formation by monocyte-activator functionalized graphene oxide *in vivo*, Nanoscale 11 (41) (2019) 19408–19421.
[78] E. Perevedentseva, S.F. Hong, K.-J. Huang, I.T. Chiang, C.Y. Lee, Y.T. Tseng, et al., Nanodiamond internalization in cells and the cell uptake mechanism, J. Nanoparticle Res. 15 (2013) 1834.
[79] O. Faklaris, D. Garrot, V. Joshi, F. Druon, J.-P. Boudou, T. Sauvage, et al., Detection of single photoluminescent diamond nanoparticles in cells and study of the internalization pathway, Small 4 (12) (2008) 2236–2239.
[80] J. Deguine, G.M. Barton, MyD88: a central player in innate immune signaling, F1000Prime Rep 6 (2014) 97.
[81] L.C. Platanias, Mechanisms of type-I- and type-II-interferon-mediated signaling, Nat. Rev. Immunol. 5 (5) (2005) 375–386.
[82] S. Revu, J. Wu, M. Henkel, N. Rittenhouse, A. Menk, G.M. Delgoffe, et al., IL-23 and IL-1beta drive human Th17 cell differentiation and metabolic reprogramming in absence of CD28 costimulation, Cell Rep. 22 (10) (2018) 2642–2653.
[83] V. Santarlasci, L. Cosmi, L. Maggi, F. Liotta, F. Annunziato, IL-1 and T Helper immune responses, Front. Immunol. 4 (2013) 182.
[84] J. Wang, A. Ioan-Facsinay, E.I. van der Voort, T.W. Huizinga, R.E. Toes, Transient expression of FOXP3 in human activated nonregulatory CD4+ T cells, Eur. J. Immunol. 37 (1) (2007) 129–138.
[85] G. Arango Duque, A. Descoteaux, Macrophage cytokines: involvement in immunity and infectious diseases, Front. Immunol. 5 (2014) 491.
[86] H.M. Algood, P.L. Lin, D. Yankura, A. Jones, J. Chan, J.L. Flynn, TNF influences chemokine expression of macrophages *in vitro* and that of CD11b+ cells *in vivo* during Mycobacterium tuberculosis infection, J. Immunol. 172 (11) (2004) 6846–6857.
[87] I.S. Afonina, C. Muller, S.J. Martin, R. Beyaert, Proteolytic processing of interleukin-1 family cytokines: variations on a common theme, Immunity 42 (6) (2015) 991–1004.
[88] S.M. Hurst, T.S. Wilkinson, R.M. McLoughlin, S. Jones, S. Horiuchi, N. Yamamoto, et al., IL-6 and its soluble receptor orchestrate a temporal switch in the pattern of leukocyte recruitment seen during acute inflammation, Immunity 14 (6) (2001) 705–714.
[89] D.F. Fiorentino, A. Zlotnik, T.R. Mosmann, M. Howard, A. O'Garra, IL-10 inhibits cytokine production by activated macrophages, J. Immunol. 147 (11) (1991) 3815–3822.